REPORT DOCUMENTATION PAGE

1. REPORT DATE (DD-MM-YYYY)	2. REPORT TYPE	3. DATES COVERED (From - To)
23-01-2008	REPRINT	

4. TITLE AND SUBTITLE

Satellite and ground-based observations of auroral energy deposition and the effects on thermospheric composition during large geomagnetic storms:
1. Great geomagnetic storm of 20 November 2003

5a. CONTRACT NUMBER

5b. GRANT NUMBER

5c. PROGRAM ELEMENT NUMBER
61102F

6. AUTHORS

J.H. Hecht[*], T. Mulligan[*], D.J. Strickland[**], A.J. Kochenash[**], Y. Murayama[#], Y-M. Tanaka[##], D.S. Evans[+], M.G. Conde[++], E.F. Donovan[&], F.J. Rich and D. Morrison[&&]

5d. PROJECT NUMBER
2301

5e. TASK NUMBER
SD

5f. WORK UNIT NUMBER
Z4

7. PERFORMING ORGANIZATION NAME(S) AND ADDRESS(ES)

Air Force Research Laboratory /VSBXP
29 Randolph Road
Hanscom AFB, MA 01731-3010

8. PERFORMING ORGANIZATION REPORT NUMBER

AFRL-RV-HA-TR-2008-1002

9. SPONSORING/MONITORING AGENCY NAME(S) AND ADDRESS(ES)

10. SPONSOR/MONITOR'S ACRONYM(S)
AFRL/VSBXP

11. SPONSOR/MONITOR'S REPORT NUMBER(S)

12. DISTRIBUTION/AVAILABILITY STATEMENT

Approved for Public Release; distribution unlimited.

13. SUPPLEMENTARY NOTES

14. ABSTRACT

The great geomagnetic storm of 20-21 Nov, 2003 was associated with the passage of magnetic cloud past the earth. The changes in thermospheric composition and particle precipitation are compared to those observed during geomagnetic activity on 17 November 2003, and during the intervening quieter period. We used data from (1) ground-based magnetometers, an imaging riometer, a scanning Doppler imaging Fabry-Perot, and photometers from stations in Alaska, (2) photometers from Canadian sites, (3) NOAA POES and DMSP particle sensors, and (4) the TIMED Global Ultraviolet Imager far UV sensor. Composition changes associated with the input of auroral particle and Joule energy showed larger depletions in atomic oxygen on 20 Nov than on the other nights and greater changes than are seen in the Naval Research Lab Mass Spectrometer and Incoherent Scatter (NRLMSIS) model atmosphere. NRLMSIS does better in reproducing the changes during the great magnetic storm with long duration auroral energy input than during the shorter time duration that occurred on 17 Nov. During the nights with the largest changes in composition the input of Joule energy dominates over auroral particle energy. It is shown that the particle energy distributions associated with the 20-21 Nov. storm in the period around and after the passage of the magnetic cloud had lower average energies than on preceding days

15. SUBJECT TERMS

Thermosphere   Ionosphere   DMSP   Geomagnetic storm

16. SECURITY CLASSIFICATION OF:			17. LIMITATION OF ABSTRACT	18. NUMBER OF PAGES	19a. NAME OF RESPONSIBLE PERSON
a. REPORT	b. ABSTRACT	c. THIS PAGE			Frederick J. Rich
UNCL	UNCL	UNCL	UNL	29	19B. TELEPHONE NUMBER (Include area code)

Block 13 (continued)
[##]Transdisciplinary Research Integration Center, National Institute of Information and Communications Technology, Tokyo, Japan

[+]NOAA Space Environment Laboratory, Boulder, Colorado

[++]Geophysical Institute, University of Alaska Fairbanks, Fairbanks, Alaska

[&]Physics Department, University of Calgary, Calgary, Alberta, Canada

[&&]Johns Hopkins University Applied Physics Laboratory, Laurel, MD

Satellite and ground-based observations of auroral energy deposition and the effects on thermospheric composition during large geomagnetic storms:
1. Great geomagnetic storm of 20 November 2003

J. H. Hecht,[1] T. Mulligan,[1] D. J. Strickland,[2] A. J. Kochenash,[2] Y. Murayama,[3] Y.-M. Tanaka,[4] D. S. Evans,[5] M. G. Conde,[6] E. F. Donovan,[7] F. J. Rich,[8] and D. Morrison[9]

[1] This report describes thermospheric composition and particle precipitation changes that occurred during the period of the great geomagnetic storm of 20–21 November 2003, an event that was associated with the passage of a magnetic cloud past the Earth. These changes are compared to those observed during geomagnetic activity on 17 November 2003 and during the intervening quieter period. The data used are obtained from (1) ground-based magnetometers, an imaging riometer, a scanning Doppler imaging Fabry-Perot, and photometers from stations in Alaska, (2) photometers from Canadian sites, (3) NOAA POES and DMSP particle sensors, and (4) the TIMED Global Ultraviolet Imager far UV sensor. The composition changes associated with the input of auroral particle and Joule energy showed larger depletions in atomic oxygen on 20 November than on the other nights and greater changes than are seen in the Naval Research Laboratory Mass Spectrometer and Incoherent Scatter (NRLMSIS) model atmosphere. NRLMSIS does better in reproducing the changes during the great magnetic storm with its long duration auroral energy input than during the shorter time duration geomagnetic activity that occurred on 17 November. During the nights with the largest changes in composition the input of Joule energy dominates over auroral particle energy. It is shown that the particle energy distributions associated with the 20–21 November storm in the period around and after the passage of the magnetic cloud had lower average energies and were enhanced at energies below 0.1 keV than those that caused auroral displays on the preceding days.

1. Introduction

[2] Geomagnetic auroral superstorms are rare events with only a few occurring during each 11 year solar cycle [*Vallance Jones*, 1992]. Because of their rarity and the large amount of solar energy that moves to the Earth from the Sun there is great interest in understanding the nature of these storms from birth to death throughout the entire Sun-Earth connection region. With each successive solar cycle more data on such storms are acquired as an increasing array of ground- and space-based assets are deployed. During this solar cycle, number 23, several large geomagnetic storms have already occurred. Two of these are within 1 month of each other in October and November 2003, and they have already been the subject of numerous studies, taking advantage of these observational assets, which were reported in a special issue of JGR [*Gopalswamy et al.*, 2005a].

[3] In Situ Mass Spectrometer satellite measurements have historically been the largest database for information

[1]Space Science Applications Laboratory, The Aerospace Corporation, Los Angeles, California, USA.
[2]Computational Physics Inc., Springfield, Virginia, USA.
[3]Applied Electromagnetic Research Center, National Institute of Information and Communications Technology, Tokyo, Japan.
[4]Transdisciplinary Research Integration Center, Research Organization of Information and Systems, Tokyo, Japan.
[5]NOAA Space Environment Laboratory, Boulder, Colorado, USA.
[6]Geophysical Institute, University of Alaska Fairbanks, Fairbanks, Alaska, USA.
[7]Physics Department, University of Calgary, Calgary, Alberta, Canada.
[8]Air Force Research Laboratory, Hanscom Air Force Base, Massachusetts, USA.
[9]Johns Hopkins University Applied Physics Laboratory, Laurel, Maryland, USA.

about composition changes in the thermosphere during geomagnetic activity. In particular, the Atmospheric Explorer series sampled down to 135 km altitude and data from this series of measurements form an important database, which is incorporated into the Mass Spectrometer and Incoherent Scatter (MSIS) series of model atmospheres [*Hedin*, 1983]. These and similar satellite data have been used also for many individual studies during both geomagnetically quiet and disturbed periods [e.g., see *Nier et al.*, 1976; *Kayser and Potter*, 1976; *Prölss*, 1980]. These data, however, only provide a snapshot of the effects of auroral energy input at any one location and these data have not been available for many years. Recent studies have involved satellite remote sensing of far ultraviolet (FUV) emissions, which to date have mostly been confined to dayglow observations [e.g., see *Nicholas et al.*, 1997; *Strickland et al.*, 1999, 2001, 2004; *Meier et al.*, 2005; *Crowley et al.*, 2006].

[4] However, over the past 20 years there have been a number of studies which have reported the effects at night of auroral energy deposition at well-instrumented ground-based sites such as at Poker Flat, Alaska and Kangerlussuaq, Greenland [*Christensen et al.*, 1997; *Gattinger et al.*, 1991; *Hecht et al.*, 1989, 1991, 1995, 1999, 2000, 2006; *Niciejewski et al.*, 1989; *Vallance Jones et al.*, 1987]. These studies have shown that often there are large changes in atmospheric composition with only modest inputs of auroral energy. There has been only one such study of a geomagnetic superstorm, which occurred on 8–10 February 1986 [*Hecht et al.*, 1991]. During that storm there were much larger changes in the ratio of the density of atomic oxygen [O] to the density of molecular nitrogen [N_2] than were predicted by the MSIS models. At that time, however, there was only one instrumented ground-based site (Kangerlussuaq) whose data were analyzed and no attempt was made to relate those changes to auroral heating rates (local or global) or to global auroral morphology. A recent study suggests there is a relationship between local auroral heating rates and the [O/N_2] ratio, but the data are still too sparse (especially during large storms) to determine if the relationship is linear or of higher order [*Hecht et al.*, 2006].

[5] The 20 November 2003 geomagnetic superstorm is particularly interesting as it was reported to be not only the largest geomagnetic storm to date in cycle 23 with a *Dst* index of −472 nT, but it was also associated with the passage of a large magnetic cloud past the Earth [*Gopalswamy et al.*, 2005b]. Originally defined empirically in terms of in situ spacecraft measurements, magnetic clouds are observed as large transient structures in the solar wind having smoothly rotating and enhanced magnetic field vectors with low magnetic variances, decelerating speed profiles, and low plasma temperatures over intervals of many hours to several days duration [e.g., *Burlaga*, 1991]. Such periods are easily distinguished from the ambient solar wind. The simplest interpretation of the magnetic cloud structure is a cylindrical magnetic flux rope [*Mulligan and Russell*, 2001] that is either expelled from the Sun or formed during the process of a coronal mass ejection (CME). In situ observations of magnetic clouds can often be related to distinct solar ejecta [e.g., *Gopalswamy et al.*, 1998; *Webb et al.*, 2000]. In particular, magnetic clouds observed at the Earth are most notably associated with Earth-directed or "halo" CMEs seen in white light coronagraph images [*Gosling*, 1997; *Zhao and Webb*, 2003].

[6] There were many ground-based photographic observations showing significant red emission (e.g., see http://science. nasa.gov/spaceweather/aurora/gallery_01nov03_page2. html). Such observations suggest the presence of an unusual distribution of low-energy electrons well below 1 keV that are the suspected cause of the rare Type A red auroral displays [*Robinson et al.*, 1985; *Sivjee and Shen*, 1997]. An earlier study of optical emissions during the 1995 and 1997 magnetic cloud events showed they were in fact associated with the presence of low average energy electrons that are one of the hallmarks of type A red aurora [*Sivjee and Shen*, 1997; *Steele et al.*, 1998]. However, those studies were confined to a single site and only inferred average energies with no information on the energy distribution.

[7] This paper addresses several questions associated with composition change and auroral precipitation during the period around the 20 November 2003 geomagnetic superstorm. (1) Is there evidence for lower-energy electrons or other differences in the energy distribution during the 20 November superstorm as compared to the precipitation during geomagnetic substorms that occurred before and after 20 November? (2) Is there a connection between the passage of the magnetic cloud during this storm and the low-energy particle precipitation as suggested by *Sivjee and Shen* [1997] from earlier observations? (3) To what extent do the O/N_2 model (Naval Research Laboratory Mass Spectrometer and Incoherent Scatter (NRLMSIS)) predictions and actual observations agree during the period before and during the superstorm? (4) In particular, do we see any difference in O/N_2 between the model and observations during the time period of the magnetic cloud event? (5) Do any of the observed atmospheric composition changes correspond to inputs of auroral Joule or particle energy into the thermosphere?

[8] To address these questions, this study will use ground-based photometric, magnetometer, Fabry-Perot, and riometer observations from the Alaska chain in Poker Flat and Fort Yukon, photometric observations from the Canadian chain at Pinnawa and Gillam, Canada, particle observations from the Defense Meteorological Satellite Program (DMSP) J/4 and J/5 sensors aboard F15 and F16, particle observations from the Polar Orbiting Environmental Satellite (POES) Total Energy Detector (TED) [*Evans and Greer*, 2004] aboard the National Ocean and Atmosphere Administration (NOAA) 16 and 17 satellites, and FUV observations made by Global Ultraviolet Imager (GUVI) [*Christensen et al.*, 2003] aboard the Thermosphere, Ionosphere, Mesosphere, Energetics and Dynamics (TIMED) satellite. These data will be used to study the period from 17 to 21 November 2003, which is just before and during a geomagnetic superstorm.

2. Experimental Technique

[9] The approach taken in this study will be to determine composition change primarily from ground-based photometric observations from Alaska analyzed with techniques that have been used for many years [*Hecht et al.*, 2006]. The

Table 1. Geomagnetic[a] and Geographic Coordinates of Ground–Based Locations

Site	Geographic Lat	Geographic Long	Geomagnetic Lat	Geomagnetic Long
Fort Yukon	66.6	214.7	67.3	−94.7
Poker Flat	65.1	212.5	65.44	−95.66
Gillam	56.37	265.40	64.54	335.14
Pinnawa	50.15	264.12	58.48	334.19

[a]The magnetic coordinates for Poker and Fort Yukon are in the APEX system [*Richmond*, 1995]. The magnetic coordinates for Gillam and Pinnawa are in the eccentric dipole field line (EDFL) system.

average energy of the precipitating particles will be obtained from Alaska and Canadian ground-based photometric data. To obtain both quantities, typically two auroral emission ratios are measured, each sensitive to composition and average energy. *Hecht et al.* [2006] suggested a variety of auroral emission measurements could be used to obtain these quantities. For the analysis in this study a number of these techniques were used. However, during the analysis it became clear that most techniques did not provide a good measure of how the average energy of the precipitating electrons changed when low-energy particles were present in significant amounts. This, in turn, produced inaccurate estimates of composition. Thus the technique presented below is the one that both in theory and practice produced results with the least scatter and best estimate of both the energy and composition. A future publication will review the various techniques in greater detail than is presented by *Hecht et al.* [2006].

[10] However, the average energy of the precipitating particles by itself is also an important quantity to be derived for this study. This quantity can be obtained from other techniques. Thus the average energy results will be supplemented by Doppler measurements of the OI (557.7 nm) emission available at Poker Flat, imaging riometer data available at Poker Flat, J sensor and TED sensor in situ particle measurements, and TIMED observations. The energy deposited in an atmospheric column by particles and by Joule heating will be estimated from photometer and magnetometer data. Because some of these techniques are not widely known they will be described in detail below.

2.1. Ground-Based Instruments

2.1.1. Four Channel Photometers at Fort Yukon and Poker Flat Alaska

2.1.1.1. Instrument Description

[11] Two photometers, each with a four-channel filter wheel, have been deployed since 2001 at two Alaska sites, Poker Flat and Fort Yukon, whose locations are given in Table 1. The filters in each photometer are centered around the wavelength for the following auroral emissions: the (0, 1) band of the N_2^+1N system at 427.8 nm referred to as blue, OI (630.0 nm) referred to as red, OI (844.6 nm), and the (2, 1) band of the N_2 1P system at 871.0 nm. All four filters have bandwidths of between 1 and 2 nm full width at half maximum and are typically sampled every 10 s. The integration time on each filter is about 1 s. The photometers look up the local magnetic zenith and the instrument runs automatically from dusk to dawn. A version of this system has proven reliable and has been used for earlier studies [*Christensen et al.*, 1997].

[12] All emissions are corrected for backgrounds by subtracting emissions measured during periods of no aurora. Since auroral emissions can occur continuously at times, fixed backgrounds of less than 100 R are subtracted in those cases. These backgrounds are derived from previous measurements. To make sure that background variations do not add significantly to the uncertainty in the derived results, most of the analysis is restricted to periods of bright aurora where the brightness of the blue emission is above 250 R.

2.1.1.2. Analysis Technique

[13] The analysis technique to determine composition and energetics has been described in detail in several previous publications [*Hecht et al.*, 1995; *Christensen et al.*, 1997; *Hecht et al.*, 1999, 2000, 2006] and is based on producing a lookup table of predicted red, blue, and OI (844.6 nm) emissions using the Strickland electron transport code [*Strickland et al.*, 1989]. This is done by inputting a Gaussian electron energy distribution of average energy E into the top of a model atmosphere whose atomic oxygen density [O] profile is scaled by a parameter f_o. A value of one for f_o means that the [O] values are those given by the model atmosphere used by the Strickland code. Values less than one mean reduced [O]. Among the many outputs of the Strickland code are the brightnesses in Rayleighs (R) of all the auroral optical emissions as seen from the ground discussed in this paper. Four different f_o values and seven different energies form the basis of our lookup table. From the table a plot of red/blue versus OI (844.6 nm)/blue can be used to immediately determine values of E and f_o from observations of these ratios. This latter parameter, however, only makes sense if the details of the model atmosphere are known. In this work we compare not only variations during a day but also day-to-day variations and the reader may not necessarily have access to how [O] varies in each model atmosphere associated with every plot of f_o. Furthermore, we also are making comparisons with satellite dayglow results which report the quantity O/N_2 instead of f_o. Next, we show how the two approaches are equivalent and the advantages of using O/N_2, which we make use of in the remainder of the paper.

[14] To get around this limitation, we introduce O/N_2, the ratio of column densities referenced to a fixed N_2 column density (similar to referencing a quantity to a fixed pressure level). *Strickland et al.* [1995] introduced this ratio for remote sensing applications with the intended use of OI (135.6 nm) and N_2 Lyman-Birge-Hopfield (LBH) dayglow observations. The choice of the reference column density of N_2 (abbreviated to N_2 depth) is not critical but once selected, must be retained for convenient comparisons of derived O/N_2 from data set to data set. The recommended

value in the above paper is 10^{17} cm^{-2} due to slightly less scatter between OI (135.6 nm)/LBH and [O]/[N_2] than at larger or smaller reference values (scatter plots were examined from calculations utilizing an extensive set of model atmospheres). This recommended value typically occurs when the integration as a function of altitude which starts at the top of the atmosphere stops in the vicinity of 135 km. Here, we also use 10^{17} cm^{-2} but emphasize that essentially the same results follow from a value deeper in the atmosphere such as 10^{18} cm^{-2}.

[15] To clarify this, consider producing two lookup tables from the above table, one that maps the f_o grid to O/N_2 values referenced to, say, an N_2 depth of 10^{17} cm^{-2} and the other to, say, 10^{18} cm^{-2}. The tables are identical except for their O/N_2 grids. Use of the tables with optical data at a given point in time lead to two different O/N_2 values, each referenced to one of these two depths. For any given atmosphere, we now wish to know the f_o values corresponding to the just derived optical-based O/N_2 values. We first perform the integrations to obtain the O/N_2 values (call these model values) at the two depths (these correspond to f_o = 1 for that atmosphere). For each of the reference depths, the optical-based f_o is just the ratio of the optical-based O/N_2 to the model value. For the model atmosphere used to generate the tables, the two derived O/N_2 values, of course, lead back to exactly the same f_o value. For other atmospheres, the two f_o values will differ and the question is by how much. The analysis by *Strickland et al.* [1995] done for the dayglow suggests the spread in this difference is insignificant within the error budget for data and model uncertainties and is also small compared to the atmospheric variability during disturbed periods to be illustrated shortly. The uncertainty is due to the lack of knowledge as to the correct model atmosphere. For column densities of 10^{17} cm^{-2} they find uncertainties to be around two percent which is still only around 5 percent when the column density is 10^{18} cm^{-2}. These low values, which do not vary much with column density, are due to the physically constrained smooth profiles found in model atmospheres. For an auroral case this could be different. However, we will show that the choice of a model atmosphere does not significantly affect our retrievals.

[16] Note the following about this approach: (1) All auroral emissions are still calculated through the entire model atmosphere as seen from the ground. (2) The only difference from the previous approach is that now for every model atmosphere used to produce a new lookup table, the value of f_o of 1 is replaced with the calculated O/N_2 ratio. An f_o of 0.5 (for the same atmosphere) will produce an O/N_2 ratio that is half of the value for f_o of 1. (3) By using this technique, however, one would expect that the O/N_2 corresponding to an f_o of 1 for a model atmosphere during a geomagnetically quiet period would be different than the O/N_2 corresponding to an f_o of 1 for a geomagnetically disturbed period. This will be illustrated in a later section. (4) Finally, on the basis of the the error analysis by *Strickland et al.* [1995] and the above discussion, one would expect to derive for a given set of photometric data essentially the same O/N_2, independent of the model atmosphere used to derive the lookup table. This will be shown to be the case later in this paper.
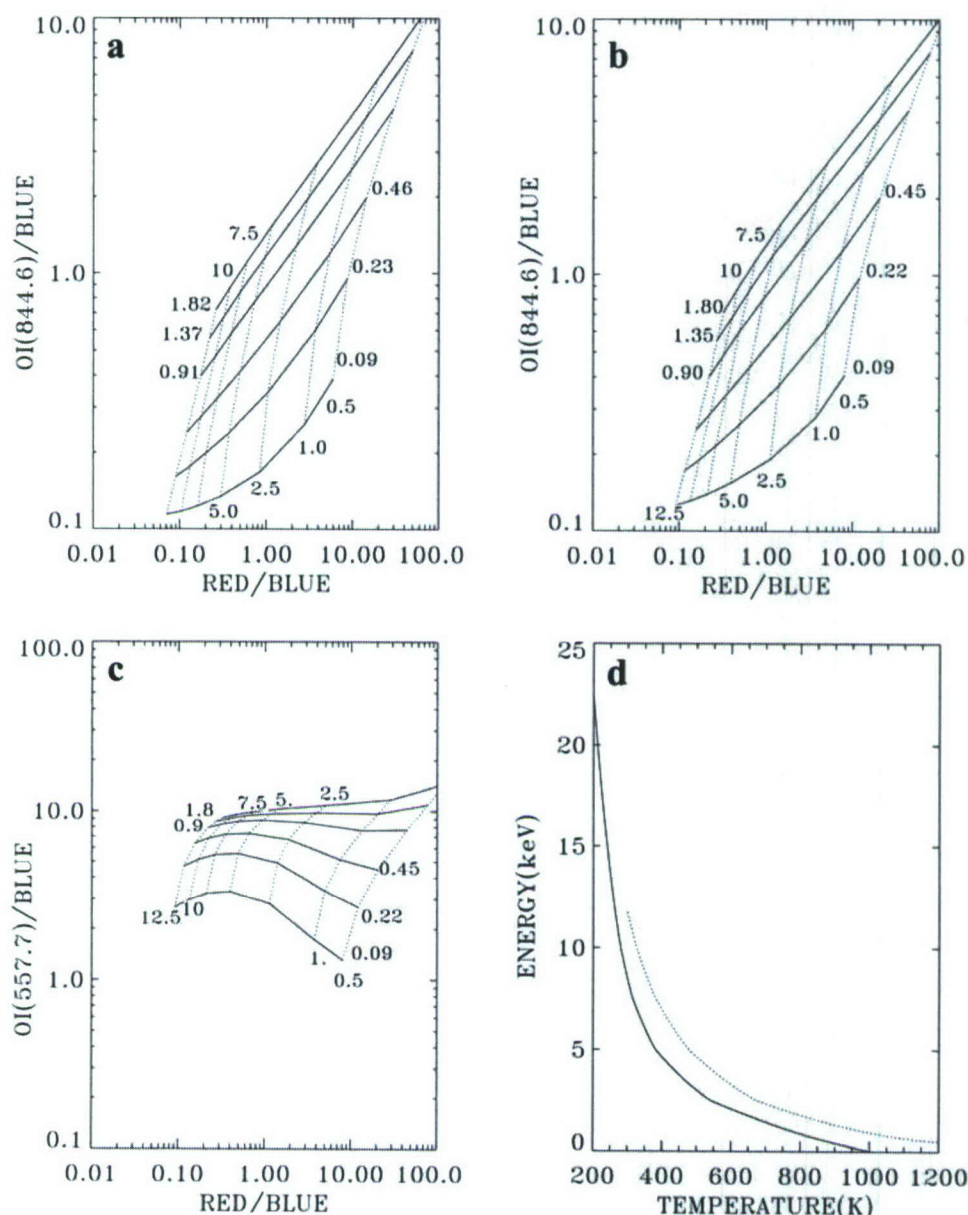
[17] Two different model atmospheres are used here in the analysis, both based on the Naval Research Laboratory Mass Spectrometer and Incoherent Scatter (NRLMSIS) model [*Picone et al.*, 2002] and both run for the location of Poker Flat. The MSIS series of models are semiempirical models that rely on physically constrained vertical profiles based on mass spectrometer and inchorent scatter radar data. NRLMSIS is an updated version of MSIS90 [*Hedin*, 1991]. For analysis on 20 November and 21 November the NRLMSIS model atmosphere used is the one appropriate to the superstorm conditions on 20 November. Thus the F10.7 and F10.7A (the 81 d average) are taken as 155.1 and 138.3, respectively, and the 3 h a_p mode is used appropriate to a universal time (UT) of 15 h. The a_p values are 150.00 (daily), 300.00 (0–3 h), 179.00(3–6 h), 94.00 (6–9 h), 94.00 (9–12 h), 12.50 (12–33 h), and 19.38 (33–59 h), where the first is the daily value and the others are the sum of the a_p values over the period prior to 1500 UT. For this model atmosphere the column O/N_2 is 0.449. Although this time period is during a superstorm, for ease of referral this is called the "disturbed" atmosphere.

[18] For analysis on 17 November and 19 November the NRLMSIS model atmosphere used is the one appropriate to the less disturbed conditions found around 1000 UT on 19 November. Thus the F10.7 and F10.7A are taken as 144.3 and 138.3, respectively, and again the 3 h a_p mode is used appropriate to a universal time of 15 h. The a_p values are 11.50 (daily), 9.00 (0–3 h), 15.00(3–6 h), 9.00 (6–9 h), 9.00 (9–12 h), 25.88 (12–33 h), and 39.00 (33–59 h), where the first is the daily value and the others are the sum of the a_p values over the period prior to 1000 UT. For this model atmosphere the column O/N_2 is 0.91. This is referred to as the "quiet" atmosphere.

[19] Figures 1a and 1b show the library of the Strickland model runs of red/blue versus OI (844.6 nm)/blue for these two atmospheres based on Gaussian energy distributions with assumed low- and high-energy tails [*Strickland et al.*, 1993]. This will be referred to as an enhanced Gaussian. For a Gaussian without tails the characteristic energy E_0 is equal to the energy of the distribution at the peak and to the average energy E of the distribution. For the particle distributions used here with tails the characteristic and average energies are the same to within 10% and thus only E will be used in the remainder of the paper. Similar plots have been presented previously [e.g., see *Hecht et al.*, 1989], which allow an easy visualization of how O/N_2 and E depend on these ratios. Solid lines show regions of constant O/N_2 and dotted lines show regions of constant E.

[20] This analysis of the photometric data assumes that the incoming electron distribution is characterized by the enhanced Gaussian. Gaussians appear to be a reasonable choice based on prior observations during large geomagnetic storms and during moderate substorm activity [*Hecht et al.*, 1991, 1999]. While Maxwellians sometimes are found, these tend to occur during diffuse aurora which usually have small energy fluxes. As will be shown later, there is some uncertainty involved in this assumption. On average for the data considered here Maxwellians increase the derived O/N_2 by 25% and the derived E by 10%. The reason for this increase, especially in O/N_2 is partly explained as follows. Strickland model results show that the centroid of emission for a Maxwellian distribution is

Figure 1. Plots of the derived O/N_2 (solid line) and E (dotted line) values using the Strickland model and various algorithms (see text), showing (a) red/blue versus OI (844.6 nm)/blue and "quiet" atmosphere, (b) red/blue versus OI (844.6 nm)/blue and "disturbed" atmosphere, and (c) red/blue versus OI (557.7 nm)/blue and "disturbed" atmosphere. Note that O/N_2 of 1.35 is not labeled. Also shown is (d) the derived E values as a function of OI (557.7 nm) temperature with solid line denoting "quiet" atmosphere and dotted line denoting "disturbed" atmosphere.

lower in altitude (where both distributions are constrained to replicate the observations). In order to replicate the observed OI(844.6nm)/blue ratio in this situation, the Gaussian-based O density profile must be increased when switching to a Maxwellian distribution to compensate for the reduction in this ratio by moving the emission centriod downward in the atmosphere. However, there is also a technique for determining whether Gaussians are appropriate [*Christensen et al.*, 1987; *Strickland et al.*, 1994] and we will apply it at the end of the paper to show that the Gaussian assumption is reasonable.

[21] Now consider what is inferred from this technique in an extreme example when equal energy fluxes from a 10 keV and 0.5 keV enhanced Gaussian energy distributions are present for an O/N_2 ratio of 0.23. The inferred E value will be $\sim$1 keV while the O/N_2 will stay nearly the same. The inferred E value of around 1 keV is technically correct, although its use to derive, say, the electron density profile, would produce a significant error. This is due to the presence of high-energy particles going undetected.

[22] Furthering this example, consider the sensitivity of the two derived quantities when that distribution is enhanced or deficient in high- or low-energy "tails." Both the red/blue and OI (844.6 nm)/blue ratios show sensitivity to the presence of low- (below 1 keV) and high- (above 10 keV) energy electrons as these ratios change with

Table 2. Uncertainties in the Analysis of Ground-Based Data

Title	% for O/N_2	% for E
Counting Statistics	less than 5	less than 5
Model Atmosphere	5	10
Reference Depth	5	5
Energy Distribution (Maxwellian or Gaussian)	25	10
Absolute Calibration	20	20
Relative Calibration	10	10
Total Absolute	32	23
Total Relative	28	16
Total Relative with known Gaussian	12	12

E. However, using photometric data to derive E and O/N_2 will show more sensitivity to low-energy electrons. For example, consider where a case of moderate blue emission, on the order of 1000 R, and both ratios are at least 0.3 or larger. The E value will be less than 5 keV and both the red and OI (844.6 nm) emissions will be significant (300 R or much greater). In this case there will be a high sensitivity to low-energy electrons. In contrast, if both ratios are around 0.1 or less, E will be above 10 keV. This means both the red and OI (844.6 nm) emission will be small (on the order of 100 R or below). Thus the low ratios will be more affected by measurement uncertainties and background corrections in the red and OI (844.6 nm) emissions. In addition, independent of the blue emission brightness, this greater sensitivity to low-energy electrons is reflected in the composition measurement as the separation of the lines of constant O/N_2 increase toward lower energy. Thus the increasing sensitivity of both ratios to low-energy electrons means that a small enhancement of the low-energy component can be measured more easily than a high-energy enhancement resulting in a tendency to obscure the presence of high-energy particles while emphasizing the presence of a low-energy component. Nevertheless, for all but very low electron fluxes, the E values and the O/N_2 results are not much affected by uncertainties in the shape of the assumed Gaussian energy distribution.

[23] The electron flux Q can be derived from the blue intensity. Nominally, 1 mW/m^2 (1 erg-cm^{-2}-s^{-1}) of electrons produces about 250 R of blue. Since the proton flux is usually a small fraction of the electron flux and the emission efficiency for protons and electrons is similar [*Strickland et al.*, 1993], any difference between the species is ignored. The derived Q reported in this work, called Q(particle) is, except where noted, the total electron and proton flux. All plots are interpolated onto 1 min grids.

[24] In previous studies we have estimated the uncertainty to be typically less than 30% and often better than 10% [*Hecht et al.*, 2006]. However, with the comparisons we show later we can better quantify this. Table 2 lists the major sources of error and the associated effects on the derived O/N_2 and E. For absolute uncertainties, all must be considered, while for measurements of relative changes the absolute calibration is replaced by the relative calibration. Note, though, that the total uncertainties are actually for a single point as the calibration uncertainties apply to all data and do not vary from measurement to measurement. Thus the quoted total uncertainties represent an upper limit. Since a knowledge of the energy distribution is the major

unknown it appears that in a relative sense we can obtain O/N_2 to about 30% and E to about 15% if we have no knowledge of whether a Gaussian is a reasonable representation. If such knowledge is available, then these uncertainties decrease to less than 15%.

[25] However, during dynamic aurora, the error in a derived O/N_2 or E could exceed these numbers. This occurs because during the 5 s observation period the aurora changes so that the filter ratios are no longer a valid representation to be used in this analysis. Owing to this uncertainty, we will limit interpretation in the present to long period changes that occur over tens of minutes rather than short-term fluctuations over a few minutes or so.

2.1.2. Meridian Scanning Photometers at Poker Flat Alaska, Gillam and Pinnawa Canada
2.1.2.1. Instrument Description

[26] The Poker Flat Observatory [*Lummerzheim et al.*, 1990] as well as two observatories in central Canada at Pinnawa and Gillam (see Table 1) have Meridian Scanning Photometers (MSP) that measure OI (557.7 nm), red and H-beta (486.1 nm). At Poker the MSP measures blue while the MSPs at Pinnawa and Gillam measure the (0,2) band of the N_2^+1N system at 470.9 nm. The blue and the 470.9 nm bands are within the same system and their ratios are constant [*Vallance Jones*, 1974]. These measurements are made along the magnetic meridian with data samples up the magnetic zenith occurring approximately once a minute. For the Poker MSP, the data have not been recently calibrated. Thus in the analysis below the Poker MSP data will only provide information on H-beta. The H-beat data, even in a relative sense, provide insight as to correlations between the occurrence of proton aurora and changes E obtained using the photometer data described above. Furthermore, since the derived O/N_2 is sensitive to the absolute calibration, only the E results will be presented for the Canadian stations.

2.1.2.2. Analysis Technique

[27] The H-beta measurements allow a measure of proton energy flux since ~50 to 100 R of H-beta is about 1 mW/m^2 [*Vallance Jones*, 1974]. The range exists because the flux depends on the average energy of the protons [*Vallance Jones*, 1974; *Strickland et al.*, 1993]. Recent studies of satellite particle data [*Coumans et al.*, 2002] suggest average energy values well above 20 keV for protons, and thus we adopt a nominal H-beta yield of 50 R for H-beta emission for 1 mW/m^2 of incoming protons.

[28] Although the emission efficiency of OI (557.7 nm) may be higher for proton excitation than for electron excitation, this remains uncertain. Since previous workers [*Vallance Jones*, 1974] have found similar efficiencies for protons and electrons, we will adopt (as we did for the N_2 and other OI emissions) the same efficiency for proton and electron excitation.

[29] The Strickland model includes the auroral excitation and quenching of O (^{1}S) responsible for OI (557.7 nm) and as discussed by *Strickland et al.* [2000], the two main sources are direct electron impact excitation of O, and the quenching of the N_2(A) state by O. The latter mechanism dominates in the lower thermosphere where the bulk of excitation occurs under active conditions. At low O/N_2 values <0.5, OI (557.7 nm) increases with increasing O/N_2. The quenching of N_2(A) in this situation by O has a weak

impact on the $N_2(A)$ density. However, at the larger E values (e.g., >5 keV) where most of the excitation is in the lower thermosphere, OI (557.7 nm) becomes insensitive to increases in O/N_2 as it extends beyond ~1. This saturation effect arises from an increase in the O density to the point of reducing the density of $N_2(A)$ through quenching. Thus the volume excitation rate of O (^1S) for this reaction (proportional to the product of these densities) becomes effectively constant.

[30] Figure 1c shows a plot of OI (557.7 nm)/blue versus red/blue as functions of E and O/N_2 for the "disturbed" atmospheres that is used for analyzing the Canadian MSP data on 20 November. Note that the derivation of E depends greatly on the red/blue ratio. Even if an uncertain calibration produces inaccuracies in the absolute value of E, relative changes in E, which are the intended use of these data, remain accurate.

2.1.3. Scanning Doppler Imaging Fabry-Perot at Poker Flat, Alaska
2.1.3.1. Instrument Description

[31] The Scanning Doppler Imaging Fabry-Perot developed at Poker Flat Observatory, Alaska [*Conde and Smith*, 1998] measures the line profile of OI (557.7 nm) allowing an inference of E from the measured temperature. The instrument actually produces a map of the temperature over the whole sky. For this study the pixels closest to the magnetic zenith are used.

2.1.3.2. Analysis Technique

[32] As noted by *Hecht et al.* [2006], this technique provides an alternative method for deriving E and O/N_2. The Strickland model includes all relevant cross sections, chemical reactions, and quenching that produce OI (557.7 nm) and thus allows the OI (557.7 nm) Doppler temperature to be predicted for a given E.

[33] Figure 1d shows the relationship between measured temperature and E for the geomagnetically "quiet" and "disturbed" atmospheres. As this technique depends on the OI (557.7 nm) temperature, it is not very sensitive to low-energy electrons since most of the OI (557.7 nm) emission occurs in the lower E region. For the hypothetical example above of equal 0.5 and 10 keV electron energy fluxes, the inferred E value would be ~7 keV assuming the "quiet" atmosphere shown in Figure 1d. The uncertainties in the zenith temperatures are on the order of 1%, which translates into less than 0.1 keV error.

[34] There are potential problems at energies above 10 keV. First, at very high energies well above 10 keV, the emission comes from an altitude below 100 km where OI (557.7 nm) begins to be severely quenched. This is reflected in the results for the "quiet" atmosphere in which the Doppler temperature shows only small temperature changes as E approaches 25 keV. Second, dynamical effects such as gravity waves or tides are not included in the model atmosphere and these can distort the temperature profile and therefore the inferred temperature. This is especially significant when high-energy electrons are present that penetrate to around 100 km, a region known for strong wave activity and where significant OI (557.7 nm) emission can occur. In addition to these two problems, there is the possibility that the model atmosphere may simply not represent the actual atmospheric temperature profile accurately. An example of this possibility is given in a later section.

2.1.4. Magnetometers at Poker Flat and Fort Yukon, Alaska
2.1.4.1. Instrument Description and Analysis Technique

[35] Following *Duboin and Kamide* [1984] and ignoring the effect of neutral winds [*Thayer et al.*, 1995; *Thayer*, 1998], the amount of electromagnetic energy deposited in a volume per unit time is the Joule heating rate, q_j, in W/m^3. The height-integrated Joule heating rate, Q_J in units of mW/m^2, equals the rate at which electromagnetic energy is deposited into an atmospheric column [*Duboin and Kamide*, 1984; *Thayer et al.*, 1995]. Ignoring neutral winds, Q_J calculated following *Duboin and Kamide* [1984] is equivalent in units to a flux [*Thayer et al.*, 1995] and represents the electromagnetic energy deposited into the ionosphere as thermal energy [*Thayer et al.*, 1995]. However, neutral winds have an effect on this quantity as discussed by *Thayer et al.* [1995] and *Thayer* [1998]. However, even in those studies for the most part, Q_J calculated ignoring winds often provided a good proxy for the height-integrated Joule heating rate including neutral wind effects.

[36] *Duboin and Kamide* [1984] suggest that Q_J can be estimated from geomagnetic field data obtained from ground-based magnetometers. Magnetometers are present at both Alaska sites and these data have been used in previous studies to estimate Q_J [*Duboin and Kamide*, 1984; *Christensen et al.*, 1997; *Hecht et al.*, 1995, 2000, 2006]. Often Q_J well exceeds Q (particle) and thus Q_J may be the primary cause of vertical winds and subsequent composition change [e.g., see *Christensen et al.*, 1997].

[37] To obtain Q_J, we use the ΔH component from a magnetometer (i.e., the change of the H component from nominally nonauroral conditions [*Duboin and Kamide*, 1984]). The value of $(\Delta H)^2$ in units of $(nT)^2$ can be used when multiplied by a constant, 8×10^{-5} $mW/((m^2)(nT^2))$, to estimate Q_J, although this approximation may be inaccurate on occasion. In particular from their study, which took place in April 1978, *Duboin and Kamide* [1984] stated that the above constant was appropriate during nighttime periods (after about 0800 UT at Poker Flat) when ΔH was negative, indicative of a westward electrojet. During the early evening prior to 0800 UT when ΔH was positive and indicative of an eastward electrojet, the constant was found to be over 10 times larger at 105×10^{-5} $mW/((m^2)(nT^2))$. For the vast majority of data presented in this study, the lower value is used, although we have used the higher constant where appropriate.

[38] In a previous study, comparisons have been made during nighttime auroral activity between Q_J calculated from radar data at Kangerlussuaq, Greenland and the approximation to Q_J used in this paper [*Hecht et al.*, 2000]. The use of the lower constant approximation for periods of negative ΔH was found to provide a good approximation to Q_J independent of the original analysis by *Duboin and Kamide* [1984].

2.1.5. Imaging Riometer at Poker Flat, Alaska
2.1.5.1. Instrument Description

[39] A riometer observes ionospheric absorption of radio noise (called cosmic noise absorption; CNA), which is used to infer the lower ionospheric electron density variation. A riometer generally operates at frequencies of 20 to 50 MHz. Observed from the ground, cosmic radio noise is partially

absorbed by the ionosphere in the 80–90 km altitude range and the amount of the radio absorption will vary depending on ionospheric conditions. Disturbances in electron density in the lower ionosphere can be measured by observing the variation of this cosmic noise intensity on the ground. In polar regions aurora is one of the events which can cause CNA variation.

[40] The imaging riometer at Poker Flat has been in continuous operation since October 1995 and it consists of a 16×16-element square array antenna, a Butler matrix, 16 receivers, and personal computers for system control. The imaging riometer scans an antenna beam in about 200 directions within 1 s to monitor cosmic radio noise variation at 38.2 MHz over a wide field of view of the radio sky. It observes lower ionospheric disturbances over a 400-km by 400-km field of view at the 90-km height with a spatial resolution of about $7°$ (11 km around the zenith), a sensitivity better than 0.1 dB, and a time resolution of 1 s [*Murayama et al.*, 1997; *Mori et al.*, 2004].

2.1.5.2. Analysis Technique
[41] For data analysis in this work, we use the mean value of CNA for the two beams closest to the geomagnetic zenith. The presence of CNA suggests that high-energy electrons are involved, since electron energies greater than 25 keV are required to penetrate down to altitudes where CNA occurs. *Kosch et al.* [2001] and *Mori et al.* [2004] have recently discussed the utility of using imaging riometers to determine E based on the relationship that E is proportional to Ab/Q(particle)$^{0.5}$ where Ab is the measured riometer absorption in decibels. Thus combining Q(particle) values derived from the photometer data and Ab from the riometer data allow another measure of E, albeit one sensitive to high-energy but not low-energy tails. Because of the proportionality, an unknown, arbitrary fixed scaling factor must be applied and this is done by scaling the riometer results by a factor of 20. This factor was chosen to provide a reasonable agreement with the SDI-derived E values on 17 November. The use of a scaling factor, however, only affects the absolute comparisons and not the relative comparisons with other instruments.

[42] Continuing the same example used for the previous techniques, the riometer would infer an E of 7 keV as Q would double and Ab would essentially stay the same. We note that the radio star (Cassiopeia-A) is located just on the geomagnetic zenith (beam number [N9E8]) at 0600–0700 UT during 17–21 November 2003. This means CNA around 0500–0800 UT may be affected by the scintillations and the large source signal of this radio star.

2.2. Space-Based Instruments
2.2.1. POES Particle Detectors
2.2.1.1. Instrument Description and Analysis Technique
[43] The NOAA-16 and NOAA-17 POES satellites each include a Total Energy Detector (TED) instrument that measures the proton and electron flux in a number of channels from 50 eV to 20 keV. Unfortunately, not all data are sent down and the data used in this study are the ratios of the omnidirectional electron energy flux below 1 keV to the total electron energy flux and the ratio of the proton to electron energy flux. Because much of the proton flux

occurs above 30 keV [*Coumans et al.*, 2002], we also add to the TED proton flux that measured by the Medium Energy Proton and Electron Detector (MEPED) (part of the MEPED/TED package), which measures proton energies from 30 keV to 1000 keV. In November 2003 the Local Time Ascending Node (LTAN) for NOAA-16 was 1409 LST and for NOAA-17 was 2219 LST. LTAN is the local solar time (LST) at the subsatellite point when the satellite crosses the equator northbound. Typical times for passing over or close to a polar northern hemisphere site such as Poker Flat Alaska at night will be quite different for the different satellites. On 20 November 2003 a NOAA-17 northbound pass came within $3°$ of Poker Flat at 0702 UT (2102 LST) during the early evening. A NOAA-16 southbound pass also came within $3°$ of the same site at 1311 UT (0327 LST) in the postmidnight sector.

2.2.2. DMSP Particle Detectors
2.2.2.1. Instrument Description and Analysis Technique
[44] The DMSP F15 and F16 satellites each carry a particle detector, J/4 on F15 and J/5 on F16. F15 has an LTAN of about 2110 LST while F16 has an LTAN of about 1954 LST. On 20 November 2003 the closest F15 and F16 nighttime passes to Poker Flat occurred near the Alaska-Canada border at 0522 and 0350 UT, respectively. Both were between sunset and midnight local time. The two J sensors differ in that the J/5 sensor has a wider field-of-view and can obtain direction information for precipitating particles, while the J/4 sensor looks only into the zenith direction. For the purposes of this work, the J/5 and J/4 data both are presented as flux integrated over the downward hemisphere, assuming the flux is independent of pitch angle. Each J sensor has 19 energy channels for electrons and another 19 energy channels for protons, covering the 30 eV to 30000 eV energy range. In this study we sum these flux values to form three energy channels from 30 to 100 eV, 100 to 1000 eV, and above 1000 eV. This allows a more precise measurement of the contribution of particles with energies below 100 eV, which are especially important in the production of the rare type A red aurora [*Robinson et al.*, 1985].
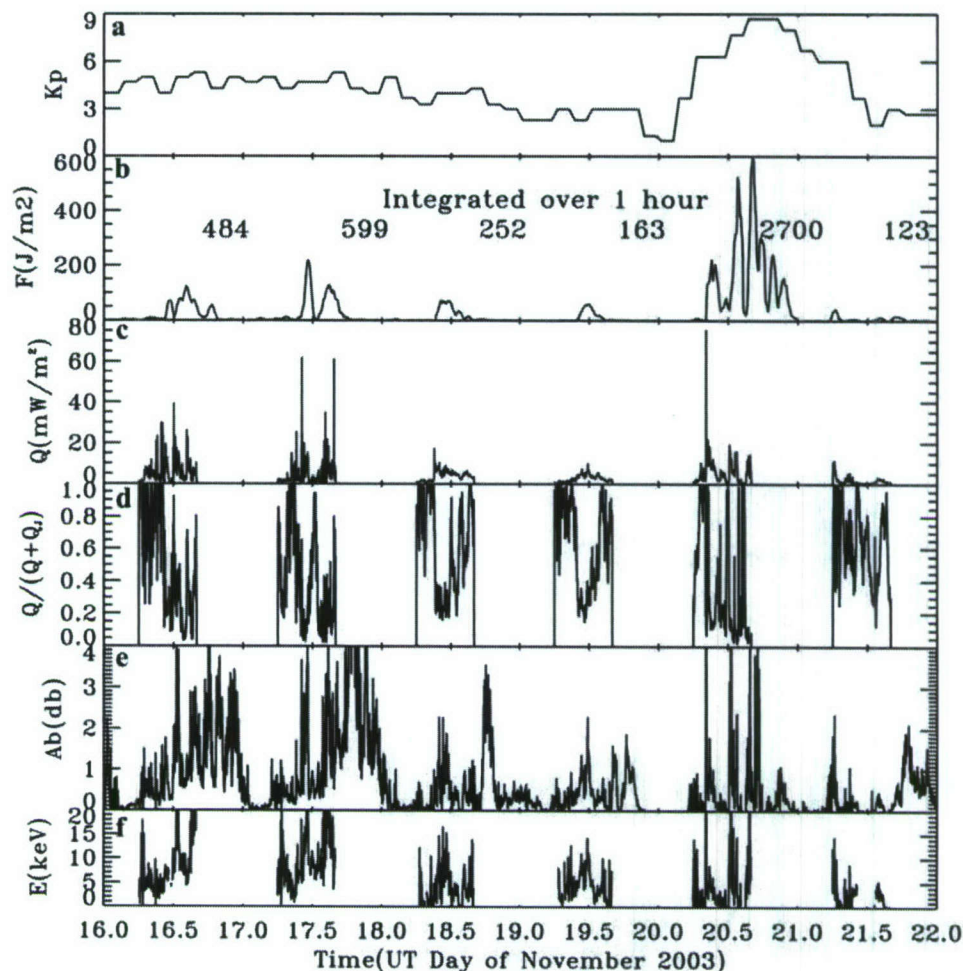
2.2.3. GUVI
2.2.3.1. Instrument Description
[45] One of the four instruments aboard the NASA TIMED satellite is the Global Ultraviolet Imager (GUVI), an imaging spectrograph capable of making global maps in five FUV colors: Lyman-alpha at 121.6 nm, OI at 130.4 nm and 135.6 nm, and two portions of the N_2 Lyman-Birge-Hopfield (LBH) band system, LBH short wavelength (designated LBHs) at 141–153 nm, and LBH long wavelength (designated LBHl) at 167 to 181 nm. While the pixel sizes are quite small on the ground (less than 10×10 km for nadir pixels), in this work they are binned to approximately 35 by 35 km to increase the sensitivity. A full description of the instrument is given by *Christensen et al.* [2003].

2.2.3.2. Analysis Technique
[46] Ratios of the maps of the OI (135.6 nm) to LBHs colors provide a measure of O/N_2 when these data are obtained from the dayglow [*Strickland et al.*, 1995, 2004]. The quiet-time analysis by *Strickland et al.* [2004] has been

Figure 2. Plots of various quantities as a function of UT from the period of 0000 UT on 16 November 2003 to 2400 UT on 21 November 2003. Poker Flat optical data are only available during the night. Shown are (a) K_p and (b) the fluence, F_J over Poker Flat derived by integrating Q_J heating rate over the preceding hour. For the 6 d the daily electromagnetic energy fluence (derived by integrating Q_J over the entire 24 h) is shown as the series of numbers in the upper part of the panel. Also shown is (c) Q(particle), designated here as Q_p, over Poker Flat derived from the blue photometer data; (d) the ratio of the Q_p to Q_T over Poker Flat; (e) Poker Flat Riometer absorption (Ab), in decibels, from the imaging riometer; and (f) the average energy of the precipitating particles derived from the Poker Flat riometer and photometer data.

extended for this November 2003 storm period by *Meier et al.* [2005] and *Crowley et al.* [2006]. However, a variation of the ground-based photometric (red/blue versus OI(844.6 nm)/blue) technique discussed above can also be used in the auroral zone on the nightside to obtain E and Q(particle). The ratio of LBHs to LBHl gives E while either one of the three channel brightness gives Q(particle). However, the E algorithm is not valid for values below 2 keV.

3. Results

3.1. Overview

[47] A superstorm occurred from about 0800 UT on 20 November 2003 to ~0800 UT on 21 November 2003. Although the day before the storm was geomagnetically quiet, a few days before that there was some geomagnetic

storm activity. To provide a context for the period from 0000 UT on 16 November to 2400 UT on 21 November, Figure 2 shows the K_p index, the total energy deposited in an atmospheric column due to Joule heating with Q_J integrated over the previous hour from the Poker Flat magnetometer data, Q(particle) from the blue emission, the ratio of Q(particle) to the sum of Q(particle) and Q_J, the Poker Flat imaging riometer absorption (Ab), and E derived from combining the riometer Ab and Q(particle) data as described above with the factor of 20 scaling factor applied as discussed earlier.

3.1.1. K_p

[48] The K_p data in Figure 2a shows that significant magnetic activity occurred on 16 November and 17 November, which decreased on 18 November and 19 November. The lowest value of K_p occurred around 2400 UT on

19 November. A large geomagnetic storm occurred on 20 November with K_p values of 8.7. The storm activity was still present through the first third of 21 November with activity decreasing throughout the rest of that day.

3.1.2. Electromagnetic Energy Fluence

[49] For a typical substorm time interval of 1 h, the total amount of electromagnetic energy deposited in a column over that time interval is derived by integrating Q_J over the preceding 1 h. Since Q_J has the same units as a flux and the time integral of a flux is a fluence, in this paper this integral will be referred to as the fluence, F_J. The advantage of plotting F_J rather than Q_J is that geomagnetic storm events of equal Q_J will differ in F_J if one event lasts longer than the other. A plot of F_J also shows the potential relation between composition change and energy deposition in the column. This allows comparison between the energy deposited in a column by Joule heating and particle heating.

[50] In evaluating plots of F_J, the following should be noted: if the substorm or storm event lasts less than 1 h (assuming a constant Q_J) then the total time when F_J is above zero will be 1 h or greater. If the event lasts 1 h then the peak in F_J occurs at the end of the event. For events lasting less than 1 h, the highest value in F_J represents the column energy deposition during the event. If the event lasts longer than 1 h, the peak in F_J represents a lower limit to the energy deposition.

[51] The data in Figure 2b are from the Poker Flat magnetometer and as expected typically show a peak in the postmidnight sector. The peak values are larger on 16–17 November than on 18–19 November. The largest values occur on 20 November during the storm. Interestingly, low values occur on 21 November.

[52] Also shown as numbers are the total electromagnetic energy deposited in a column for each day (F_{Jday}), derived by integrating Q_J over the entire 24 h period. These results allow a comparison of energy deposition due to the longer-lasting storm events. These values scale with K_p except as noted on 21 November where F_{Jday} is the lowest of this period.

3.1.3. Q(particle)

[53] The data in Figure 2c are derived from the Poker Flat blue emission available only at night. Q(particle) values are larger on 16–17 November than on 18–19 November, as expected. While the Q(particle) values on 20 November appear comparable to those of the other storm nights 16–17 November, Q(particle) on 21 November is low. Note that for comparisons with F_J shown later, we define F_P to be the time integration of Q(particle) over 1 h.

3.1.4. Q(particle)/Q_T

[54] Figure 2d shows the Q(particle) percentages of total energy flux Q_T derived by adding Q(particle) and Q_J. Q(particle) is often much smaller than Q_J. For cases of significant Q_T over timescales of several minutes or more, the amount due to Q(particle) is generally less than half. For example on 20 November there is a single large spike in Q(particle) that reaches 80 mW/m². However, during the rest of the night even though Q(particle) is above 5 mW/m², Q_J is larger than Q(particle) most of the time.

3.1.5. Riometer Absorption and Relative Energy

[55] One aspect of this study is to determine whether the storm on 20 November shows a different E than on other nights of this period. The riometer absorption (Ab) data shown in Figure 2e does show a significant difference. Since

riometer absorption reflects the presence of high-energy particles, it is clear that observations on 20 November do not resemble those on 16 November or 17 November, and in fact 20 November shows less absorption than on either of those days. The derivation of the average electron energy is shown in Figure 2f using the accepted scaling of Ab described above (E is proportional to Ab/Q(particle)$^{0.5}$). Since the derived energies are only relative, the values are scaled from 0 to 20 keV. To convert to absolute E values, a scaling factor will be used in later figures. On 16 November and 17 November there are significant periods of relatively high E particle deposition. This also appears true on 18 November and 19 November. However, while there are certainly such periods on 20 November, E appears considerably smaller during much of 20 November and 21 November.

3.1.6. NOAA POES Data

[56] Data from the NOAA-16 and NOAA-17 satellites allow a quick view of the energetics of the precipitating particles. While DMSP satellites also provide these data, the NOAA-16 satellite is able to provide data in a unique time frame, namely, the postmidnight sector near Poker Flat.

[57] Figure 3 shows all of the 2-s observations made by the NOAA-16 satellite in the northern hemisphere during the period from 0000 UT on 16 November 2003 to 2359 UT on 21 November 2003 when the electron flux Q(electron) exceeded 1 mW/m². Each observation is tagged by an event number that ranges from 1 at the beginning of the period through just over 5500 at the end of the period.
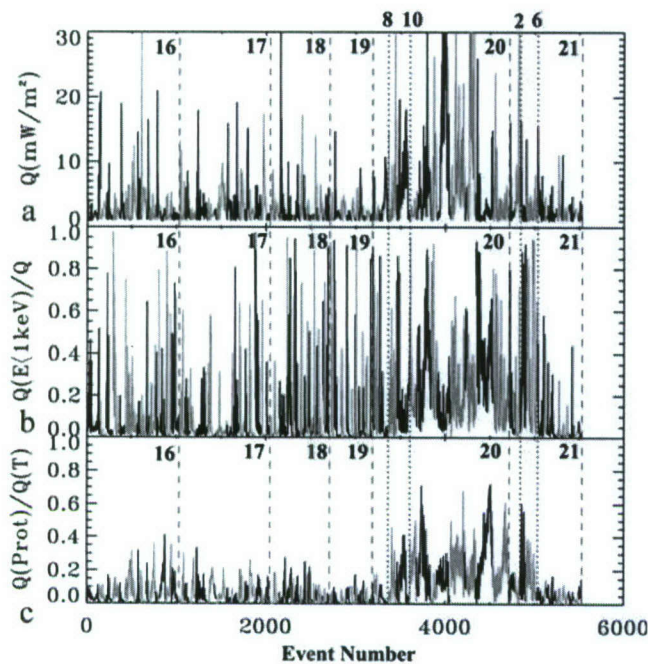
[58] To provide an indication of when these events occurred, blue vertical dotted lines mark the end of each day of observations and the day number is indicated just to the left of each line. In addition, all odd orbits are shown in black and even orbits are shown in red, making the events associated with each orbit more clearly visible. Vertical dashed lines indicate 0800 and 1000 UT on 20 November and 0200 and 0600 UT on 21 November. These are interesting periods that will be discussed later in the paper.

[59] With this approach it is easy to visualize when geomagnetic activity occurred because the most active days have the most events. Note there are many more events on 20 November than on 19 November. Furthermore, the activity on each orbit is indicated as the number of events per orbit.

[60] Figure 3a shows Q(electron) for all the events. The most geomagnetically active days 16, 17, and 20 November have, in general, higher fluxes than on the less active days 18 November and 11 November. The largest fluxes occur on the superstorm day of 20 November.

[61] Since one focus of this paper is on the energy of the precipitating electrons, Figure 3b uses TED data to show the fraction of Q(electron) due to particles with energies below 1 keV. While high ratios often exceeding 0.5 occur on all nights, there is a significant difference between the results on 20 November and on the other nights. On all other nights than 20 November the high-ratio events consist of one or two consecutive observations. This suggests the presence of narrow features, perhaps auroral arcs. However, after ~1000 UT on 20 November there are several periods during which this ratio exceeded 0.5 over many consecutive measurements. This suggests a diffuse-type enhanced, low-energy aurora consistent with the presence of Type A red aurora.

Figure 3. Plots of the number of 2 s observations when the electron flux is above 1 mW/m² for various quantities from NOAA 16 data from the period of 0000 UT on 16 November 2003 to 2400 UT on 21 November 2003 during night northern hemisphere overpasses. Each observation is tagged by an event number that ranges from 1 at the beginning of the period through just over 5500 at the end of the period. To provide an indication of when these events occurred, blue vertical dashed lines mark the end of each day of observations and the day number is indicated just to the left of each line. In addition, all odd orbits are shown in black and even orbits are shown in red. Thus the events associated with each orbit are clearly visible. Vertical dashed lines are also shown, indicating 0800 and 1000 UT on 20 November and 0200 and 0600 UT on 21 November. Shown are (a) Q(electron), (b) fraction of Q(electron) below 1 keV, and (c) ratio of Q(protons) to Q(total). Q(total) is the sum of Q(electron) and Q(proton).

[62] Even more striking is that on all the previous nights there are many periods when the ratio goes nearly to 0, indicating the presence of few low-energy electrons. The period from 0800 to 1000 UT on 20 November shows evidence of some enhanced low-energy electrons as the ratio always exceeds zero. However, after 1000 UT the low-energy component increases, resulting in a higher ratio well above zero. In fact, from 1000 UT until 2400 UT on 20 November the ratio goes close to zero only once. Thus a persistent low-energy component exists throughout this period.

[63] Figure 3c shows the other striking difference in the auroral activity on 20 November. This figure plots the ratio of the proton flux to the sum of the proton and electron flux. The proton flux is taken from the TED and MEPED instruments while the electron flux is taken from the TED instrument alone. Clearly, there is an enhanced proton component on 20 November compared to the other nights. However, a careful examination of the data does not reveal

any specific correlation between the enhanced proton component and the enhanced low-energy component. A change in the proton ratio is not necessarily correlated with a low-energy ratio.

[64] Data from NOAA-17, which samples the northern hemisphere in the premidnight sector shows similar features. However, one difference is that for NOAA-16 data, the period of 20 November is generally characterized by larger Q(electron) values than during the rest of the period. For the NOAA-17 orbit the opposite is true and the Q(electron) values are smaller on 20 November.

[65] The POES data taken together with the riometer results suggest that the large storm of 20 November was associated with lower-energy precipitating electrons. Alone these data are not able to answer the questions associated with composition change and they do not allow a continuous monitor of the electron energy distribution. To pursue this analysis requires investigation of the individual nights.

3.2. Geomagnetic Activity Prior to the Storm

[66] Data from 2 d, 17 November and 19 November, are next examined in detail. The first day represents a disturbed period when the DMSP midnight auroral boundary index (MABI) [*Rich and Denig*, 1992] showed the southern most portion of the auroral boundary to be at a magnetic latitude of 57°. On 19 November the MABI indicated quiet conditions when the boundary was at a magnetic latitude of 60° to 61°.
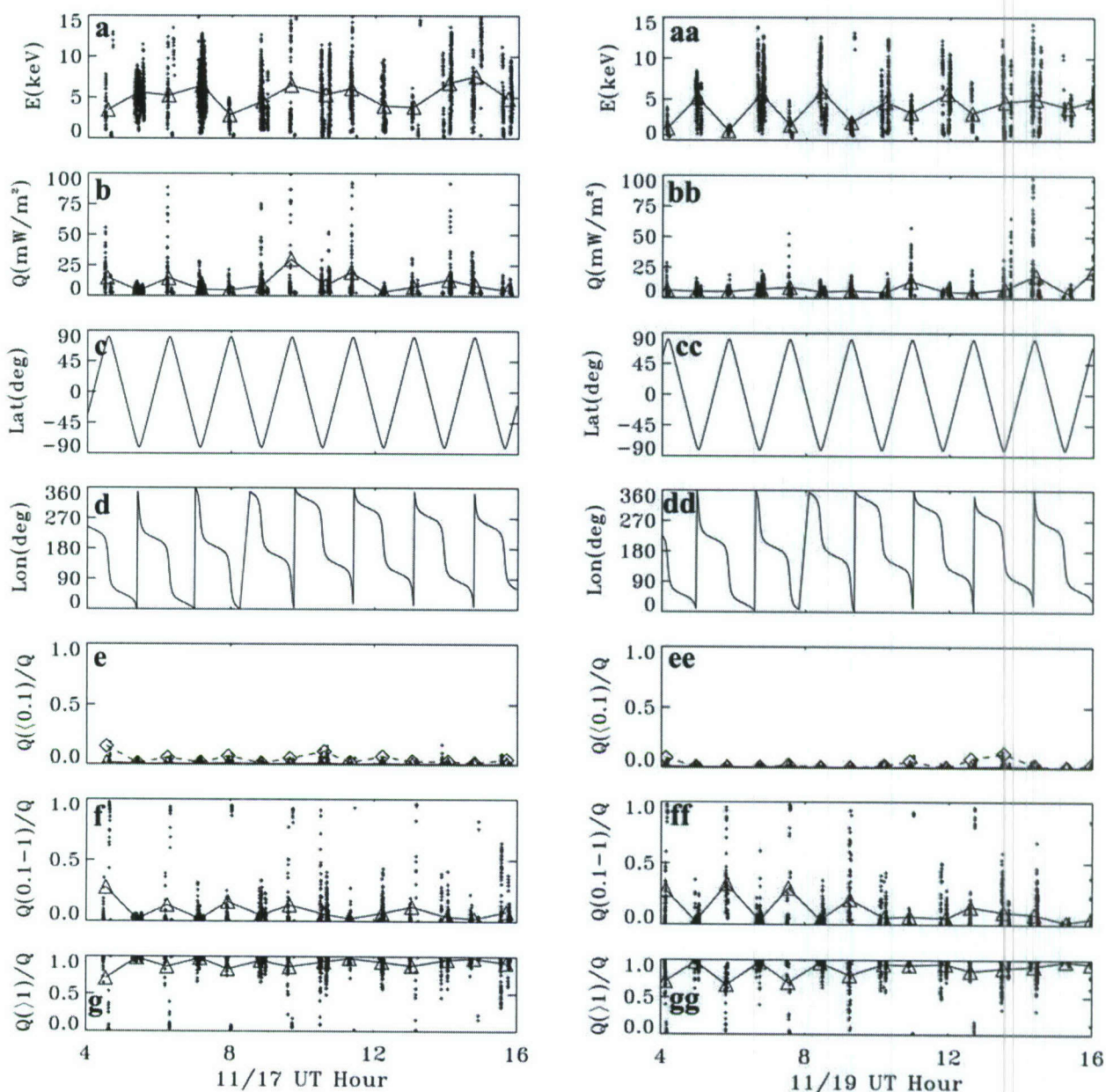
3.2.1. DMSP J Sensor F16 Data

[67] Figure 4 shows a series of plots from the DMSP F16 sensor from both 17 November (Figures 4a–4g) and 19 November (Figures 4aa–4gg). Data are restricted to events when the electron flux Q(electron) is greater than 2 mW/m². Note that unlike the POES data, here both hemispheres are shown. Figures 4c–4d and 4cc–4dd show the latitude and longitude of each pass and allow the reader to identify northern and southern polar passes.

[68] Because data are presented as a function of time, individual points (plus signs) are closely spaced data samples that to the eye appear as nearly vertical lines as the satellite quickly passes through the region of auroral precipitation in each hemisphere. A closer inspection of each pass (as shown by the vertical distribution of points) indicates there are usually two closely spaced lines representing the two passages of the auroral oval in each hemisphere. The average values are shown over each hemispheric passage as a large triangle. Solid lines connect the triangles to help guide the reader.

[69] On 17 November, the nominal E (Figure 4a) is near 5 keV while most of the flux values (Figure 4b) are below 10 mW/m². Although there is considerable spread in E, few values are at or below 1 keV and few values are at or above 10 keV. The bottom three figures (Figures 4e–4g) show the fraction of the flux below 0.1 keV, between 0.1 and 1 keV, and above 1 keV, respectively. For most of these events, on average, 80 to 95% of the flux is above 1 keV, and 5 to 20% of the flux is between 0.1 and 1 keV. In Figure 4e the solid line cannot be seen as the flux with energies below 0.1 keV is usually less than 1% of the total. This is what would be expected for Gaussian and Maxwellian particle distributions with low- and high-energy tails based on *Strickland et al.* [1993]. For this panel we plot a dashed line with large
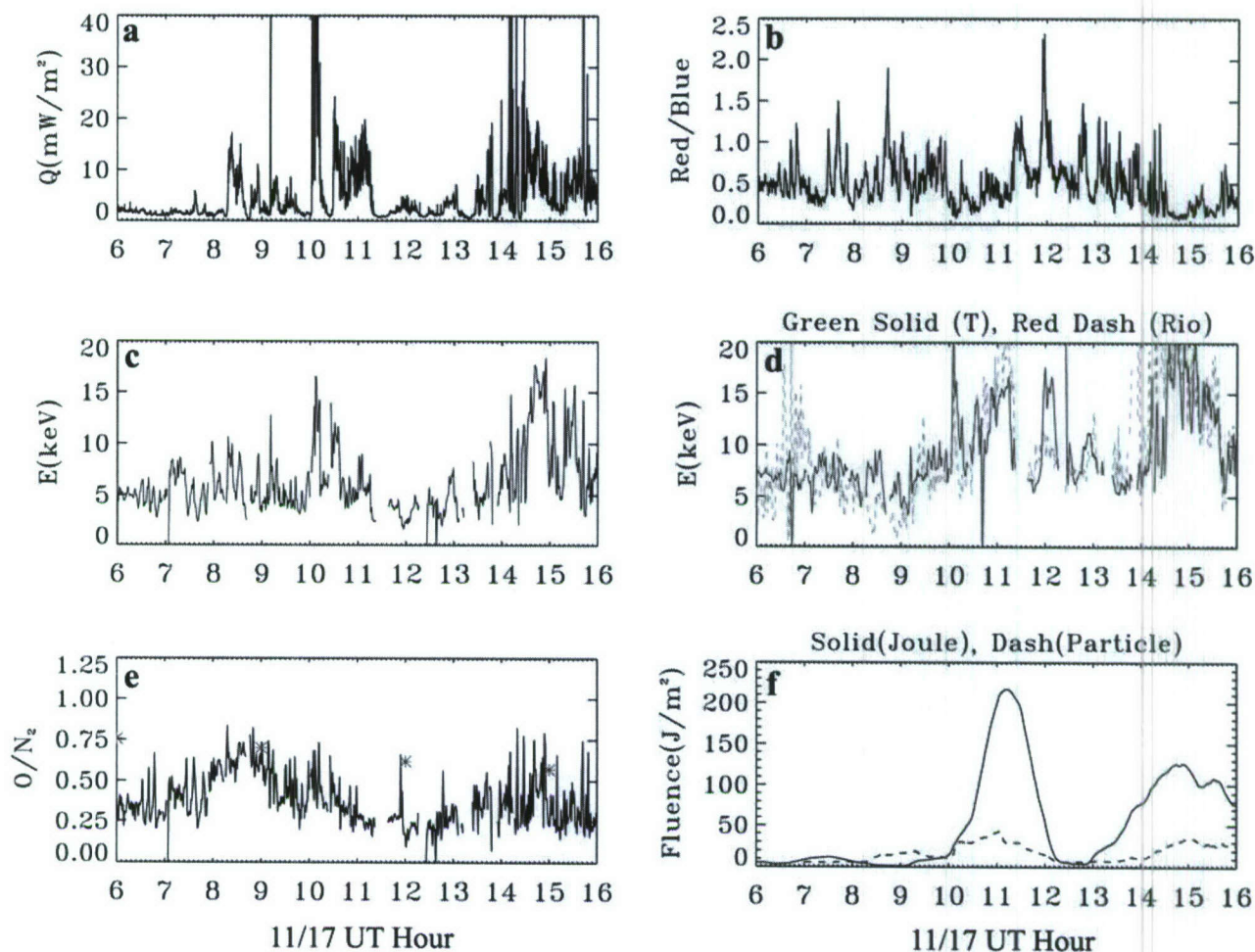
Figure 4. Plots of various quantities from DMSP F16 from the period of 0400 to 1600 UT on (left) 17 November 2003 and (right) 19 November 2003 during all times where Q(electron) is above 2 mW/m². Shown are (a) E, the average energy of the electrons (b) Q(electron), (c) latitude, (d) longitude, (e) fraction of flux below 0.1 keV, (f) the fraction of the total flux between 0.1 and 1 keV, and (g) fraction of total flux above 1 keV. (aa to gg) Same as Figures 4a–4g. For all the figures except Figures 4c, 4d, 4cc, and 4dd the average of the data over each hemispheric passage are shown as triangles (see text). The solid line is shown to guide the reader. For Figures 4e and 4ee the diamonds (connected by a dashed line) represent that fraction of the time during a hemisphere pass that the flux below 0.1 keV contributed more than 3% to the total. Note that the scales for the panels for the same quantity are the same from day to day to visually enhance any differences. See also Figure 7.

diamonds which represents the fraction of the time the flux less than 0.1 keV is 0.03 (3%) or greater of the total. (Note this plot is only valid in the interior of the diamonds which intersects the line. The line is only to guide the reader.) This 3% value was chosen because it represents a typical mean value found during the 20 November superstorm. For the night of 17 November where K_p is high this occurs only 10% or less of the time.

[70] The data from 19 November when K_p was low are similar, but there are some differences. Especially in the earlier orbits, there is a tendency for the northern and southern hemisphere passes to show different E values. They are much smaller during northern hemisphere passes. During these lower E passes the flux greater than 1 keV drops to 60% while the flux between 0.1 and 1 keV increases to 40%. This is expected as E during those passes

Figure 5. Poker Flat photometer results from 0600 to 1600 UT on 17 November 2003. Derived results are plotted when Q(particle) is above 1 mW/m². "Quiet" atmosphere results from Figures 1a and 1d are also used. Shown are (a) Q(particle), (b) red/blue, (c) E derived from red/blue versus 844.6nm/blue photometric measurements, (d) green solid line is E derived from OI (557.7 nm) temperature (Figure 1d). Red dashed line is E derived from Riometer absorption (Ab) divided by $Q^{0.5}$. Also shown is (e) O/N_2 derived from red/blue versus OI(844.6 nm)/blue (Figure 1a.) The blue stars are shown every 3 h (0600, 0900, 1200, 1500 UT) and are the NRLMSIS O/N_2 values. The first star at 0600 UT is at 0.75 and is somewhat obscured by the y axis. (f) Solid line is F_J, calculated from Q_J integrated over 1 hour. Dashed line is F_P derived from Q(particle) integrated over 1 h. Note that the scales for Figures 5a, 5c, 5d, and 5e are the same from day to day to visually enhance any differences. See Figures 6, 8, and 9.

is below 2 keV. However, the flux less than 0.1 keV still is below 1% of the total and the fraction of the time this value exceeds 3% is even lower than on 17 November.

3.2.2. Ground-Based Poker Flat Data

[71] Figures 5 and 6 show ground-based data from the Poker Flat observatory on these 2 d, 17 November and 19 November. Each figure shows data for the 2 d in the same format.
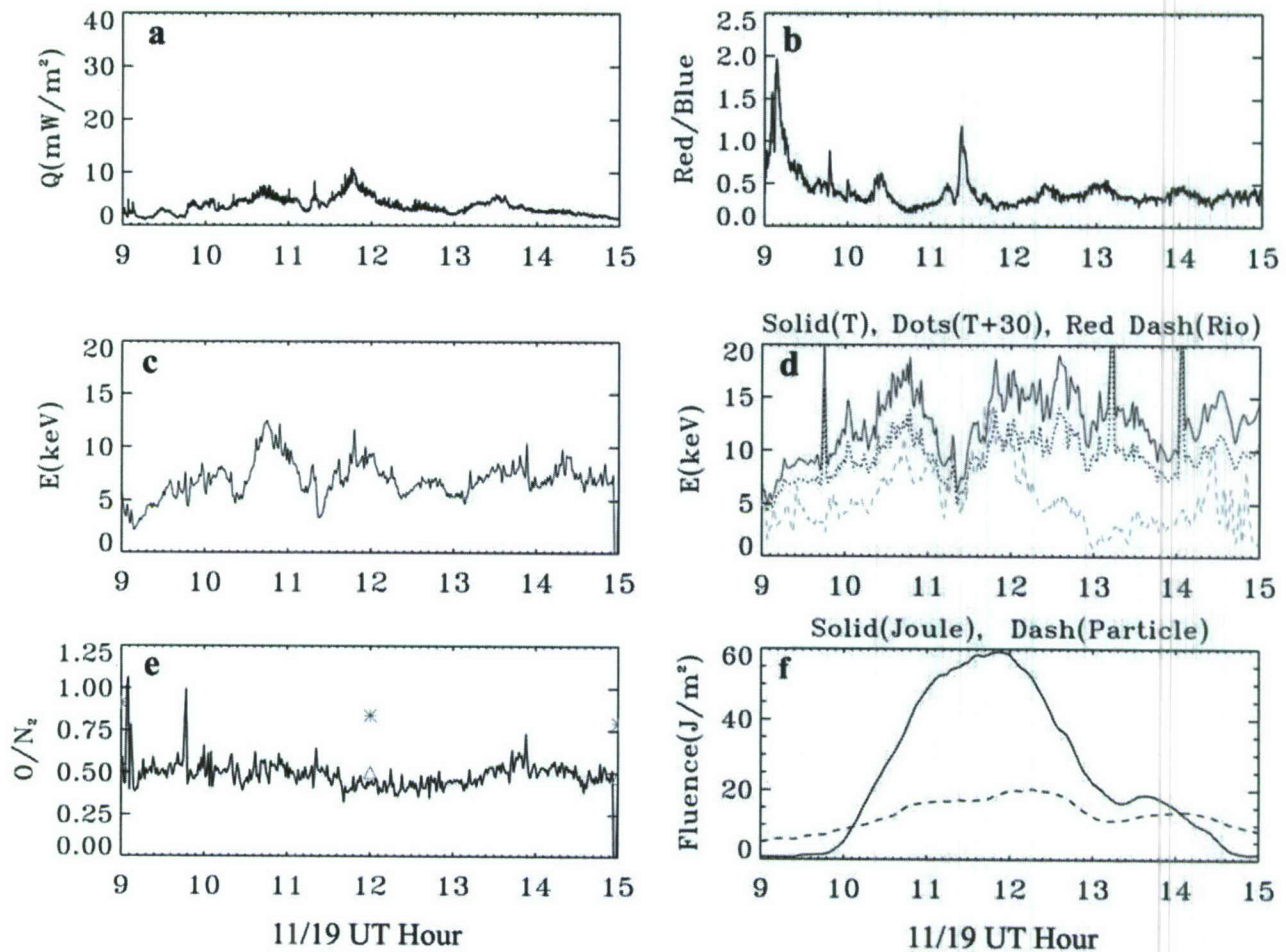
3.2.2.1. 17 November 2003

[72] Figure 5a shows Q(particle) derived from the blue photometer data. The MSP data indicate weak proton precipitation throughout this night. The particle energy flux is intense during several short periods, reaching above 40 mW/m².

[73] The red/blue ratio (Figure 5b) are mostly well below 1, suggesting moderate to high values for E. This is

confirmed in Figure 5c where the photometer-derived values (using red/blue and OI (844.6 nm)/blue and the "quiet" atmosphere) for E are almost always at 5 keV or higher, qualitatively consistent with the DMSP data.

[74] Figure 5d shows two different methods for deriving E, the first uses the OI (557.7 nm) temperature method and the second uses the combination of the riometer and photometer blue data. The riometer-derived E values $(Ab/Q^{0.5})$, when arbitrarily scaled by a factor of 20, are seen to agree very well with the temperature-derived E values. These latter results are similar but slightly higher than the results from the photometer throughout most of the night. Although all these results show that E is high (on the order 5 keV or above) there is a significant difference between the results in Figure 5c and 5d during the period 0900 to 1100 UT. During this time, a large increase in E is absent

Figure 6. Same as Figure 5 except where noted but for 19 November 2003. In Figure 6d the dotted line shows E calculated assuming the model atmosphere T is reduced by 30K. In Figure 6e the triangles (0900, 1200, and 1500 UT) represent the NRLMSIS data scaled by 0.6. These fall almost on top of, and are obscured by, both the data and by the axis at 0900 and 1500 UT. The stars, which represent the unscaled NRLMSIS results are also partially obscured at 0900 and 1500 UT by the y axis.

from the data calculated using the photometric red/blue versus OI (8444.6 nm)/blue technique. The reason for this is most probably the existence of a significant high-energy tail component in the energy distribution that is not included in the model. Recall that both the riometer and temperature techniques are sensitive to higher energy particles while the photometric technique is less sensitive. The reverse is true for low-energy tails. This result shows the advantage of having multiple measurements of the same quantity. It is also noted that for most of the 0600 to 0800 UT period, the times where interference from Cassiopeia-A might be expected, there only appears to be a small difference in the E values. However, the expected interference may be the cause of excess absorption that peaks between 0630 and 0700 UT resulting in a larger riometer-derived E value.

[75] Figure 5e shows the O/N_2 column density derived using the quiet atmosphere plots of red/blue versus OI(844.6 nm)/blue from Figure 1a. This technique should produce O/N_2 values reflective of the combined E region and F region response. Also shown in Figure 5e are the O/N_2 values from NRLMSIS calculated every 3 h. Since the model uses 3 h a_p values in its parameterization, one would not expect finer timescale variations to be present in the model predictions. However, since the actual time variations of O/N_2 are not well known, it is of interest to see if the measured variations have a shorter temporal period than 3 h. The model values do not seem to agree well in a relative sense to the O/N_2 derived from the photometer data. The model values miss the decrease in O/N_2 seen near 1200 UT. Note though that the data shown in Figure 5e are quite noisy with point to point fluctuations often exceeding the less than 5% expected from statistical fluctuations. In fact, examining the Q(particle) data from Figure 5a shows many periods during which the aurora is quite dynamic. As discussed earlier such periods can produce spurious inferences because the photometer takes several seconds to record all four channels and auroral brightness changes during that period will cause incorrect ratios to be recorded.

[76] Finally, Figure 5f shows fluences F_J and F_P from Q_J and Q (particle), respectively, derived using the previous 1 h for an integration period. Note the F_J is larger throughout most of the period. The maximum occurs when O/N_2 minimizes, consistent with previous studies [*Christensen*

et al., 1997; Hecht et al., 2006]. For this night the total electromagnetic energy fluence, derived by integrating Q_J from 0000 to 1600 UT, is about 600 J/m^2.

3.2.2.2. 19 November 2003

[77] The results for 19 November in Figure 6 simply reflect the lower-energy deposition on this night. The MSP data (not shown) again indicate weak proton precipitation. The red/blue data are generally below 1 (Figure 6b) suggesting that the photometer-derived E values (Figure 6c) are well above 2 keV, consistent with the DMSP data. In Figure 6d the riometer-derived results, which use the same scaling as in Figure 5, compare favorably with the photometer-derived results until about 1300 UT. However, after 1300 UT the riometer results show a significant decrease. The temperature-derived results for E (Figure 6d) are higher than both the riometer and photometer derived results. Reasons for this may be that the exospheric temperature is different than is assumed in the model or wave activity near 100 km exists that distorts the temperature profile. To determine the plausibility of these scenarios, the temperature profile used in Figure 1d was arbitrarily lowered by 30 degrees. The resultant E values derived from the OI (557.7 nm) temperature are shown as a black dotted line in Figure 6d. The result is a considerable reduction in the derived E, similar to the photometric results and lends credence to the suspicion that the model atmosphere may not be providing the correct temperature profile. Overall, the agreement between the temperature and photometer-derived results even after 1300 UT, and their disagreement with the riometer results suggest an absence of the very high energy electrons responsible for the riometer absorption.

[78] The O/N$_2$ column densities shown in Figure 6e indicate a small nightly variation with less than a 20% difference between the minimum and maximum. As shown by the stars, the absolute NRLMSIS results are 50% higher and when scaled (shown as triangles) the relative variation is quite similar. Note both that the variations are on the order of 10% suggested from statistics and that the Q(particle) data in Figure 6a show much less variation than on 17 November. The minimum in O/N$_2$ shown in Figure 6e occurs just after the peak of F$_J$ shown in Figure 6f. For this night the electromagnetic energy fluence Q$_J$ integrated from 0000 to 1600 UT was about 160 J/m^2. On the basis of previous results reported by Hecht et al. [2006] this low fluence is consistent with the small variation in O/N$_2$.

[79] The main puzzle is the average absolute value of O/N$_2$, which is around 0.5 compared to the model value of 0.8. The reason for this difference has not been determined but could be related to the extensive storm-related composition changes that occurred on previous nights.

3.3. Geomagnetic Activity During the Storm

[80] Next we present similar results for the two storm days, 20 November and 21 November. On 20 November the MABI indicates a major storm with a boundary ranging from a magnetic latitude of 65° prior to the storm onset around 0800 UT and dropping to about 48° at the peak of the storm. On 21 November the MABI indicates disturbed to quiet conditions with the boundary retreating from a magnetic latitude of 55° at 0000 UT to 61° later in the day.

3.3.1. DMSP J Sensor F16 Data

[81] Figure 7 shows J sensor data for these 2 d. The data are plotted in a similar manner as in Figure 4. We remind the reader that the triangles in Figures 4e and 4ee indicate the fraction of the time the flux below 0.1 keV is 0.03 or greater of the total Q.

[82] On 20 November there is considerable flux (Figure 4b) often exceeding 10 mW/m^2 throughout the day both before and after the storm onset. In fact for the pass through the auroral zones near 0813 UT, the flux reaches 75 mW/m^2 and may represent the shock discussed in the next section. The value of the average electron energy, E (Figure 4a), during the first four passes through the auroral zone are quite different between the northern and southern hemisphere. This is probably because the satellite samples local time sectors that are different in the north from the south. For the more energetic passes the averages are near 5 keV, similar to what was observed on 17 November. For the first and third more energetic passes before 0800 UT the fraction of the flux in each energy band (Figures 4e, 4f, and 4g) looks similar to the previous days, with little flux below 1 keV (less than 0.01). The fifth pass near 0800 UT is also similar, although the flux below 1 keV has slightly increased.

[83] Beginning at 1000 UT the E values drop with large fractions occurring below 1 keV. Except for the periods around 1400 and 1600 UT, the average E is at or below 2 keV with few if any points above 5 keV. However, these changes are not just because the fraction of the flux between 0.1 and 1 keV has increased while the fraction above 1 keV has decreased as was found for 19 November. Now fractions for the flux below 0.1 keV are several percent of the total, sometimes reaching 50%. The fraction of the time that the flux below 0.1 keV is 0.03 or greater is typically from 0.2 to as high as 0.8.

[84] These results show that the energy distribution is clearly different than on the previous nights for most of the period from 1000 to 2400 UT. There is not just a lower E but an enhancement in the low-energy portion of the spectrum below 0.1 keV. There is some variation, however, in the energetics. The period around 1400 and 1600 UT shows more energetic particles.
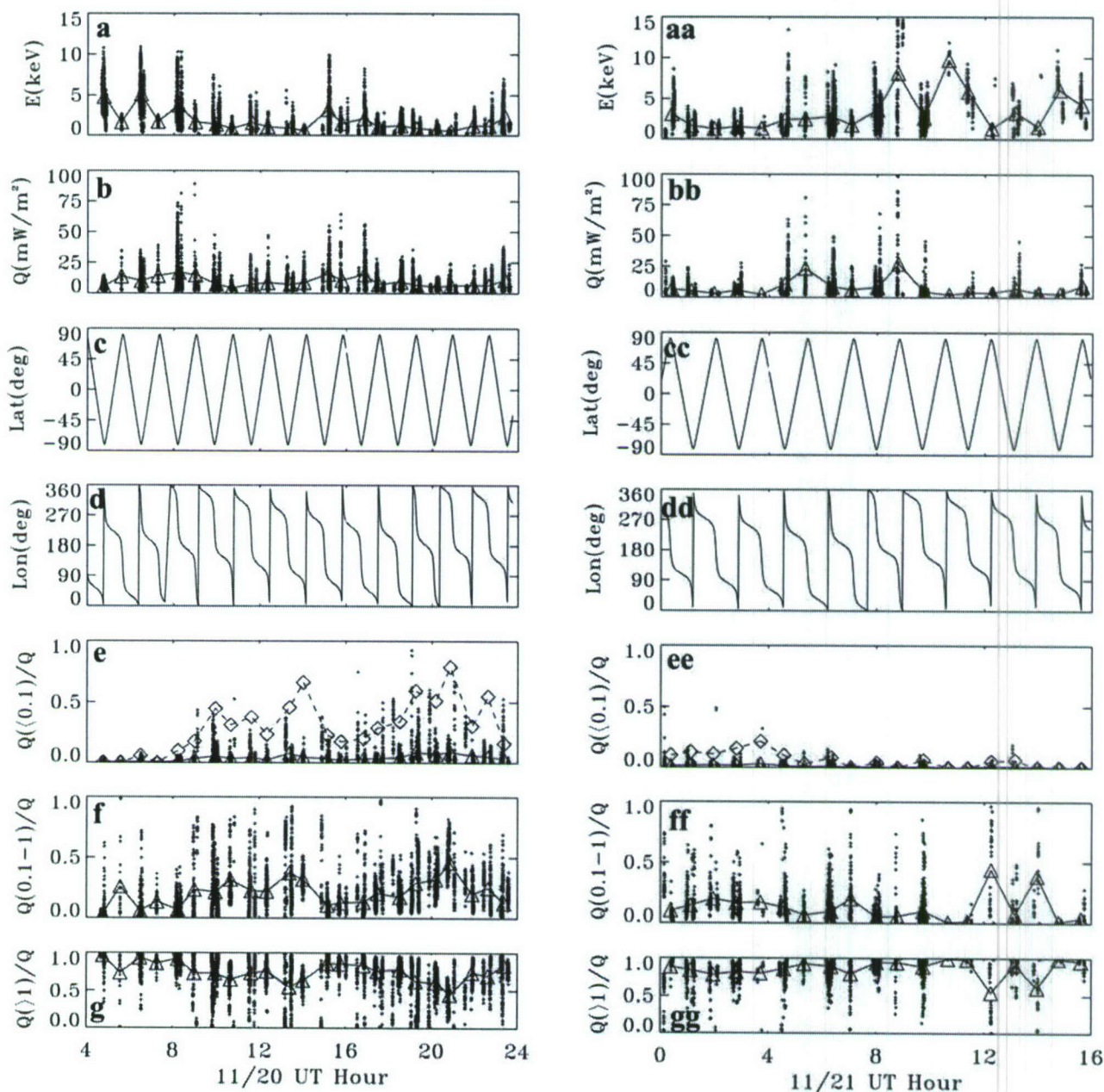
[85] The data from 21 November (Figures 4aa to 4gg) show some similarity to that on 20 November. During the period from 0000 to 0600 UT, the average E values are low, around 2 keV or less. However, the fraction of flux below 0.1 keV (Figure 4ee) does not resemble the period from 1000 to 2400 UT on 20 November. Those fractions are somewhat enhanced compared to 19 November but well below those seen on 20 November. After about 0800 UT they resemble those found on 19 November.

3.3.2. Ground-Based Poker Flat Data
3.3.2.1. Results for 20 November 2003

[86] The results shown in Figure 8 are derived using the "disturbed" atmosphere, except where noted. Figure 8a shows a large impulse of auroral energy at ~0810 UT. This is presumably related to the shock observed by SOHO at L1 at 0728 UT as reported by Gopalswamy et al. [2005b]. The transit time of the shock to the top of the magnetopause is between 30 and 60 min. After 0800 UT the particle flux decreases to a minimum around 1030 UT. There are several periods after this of intense auroral activity.
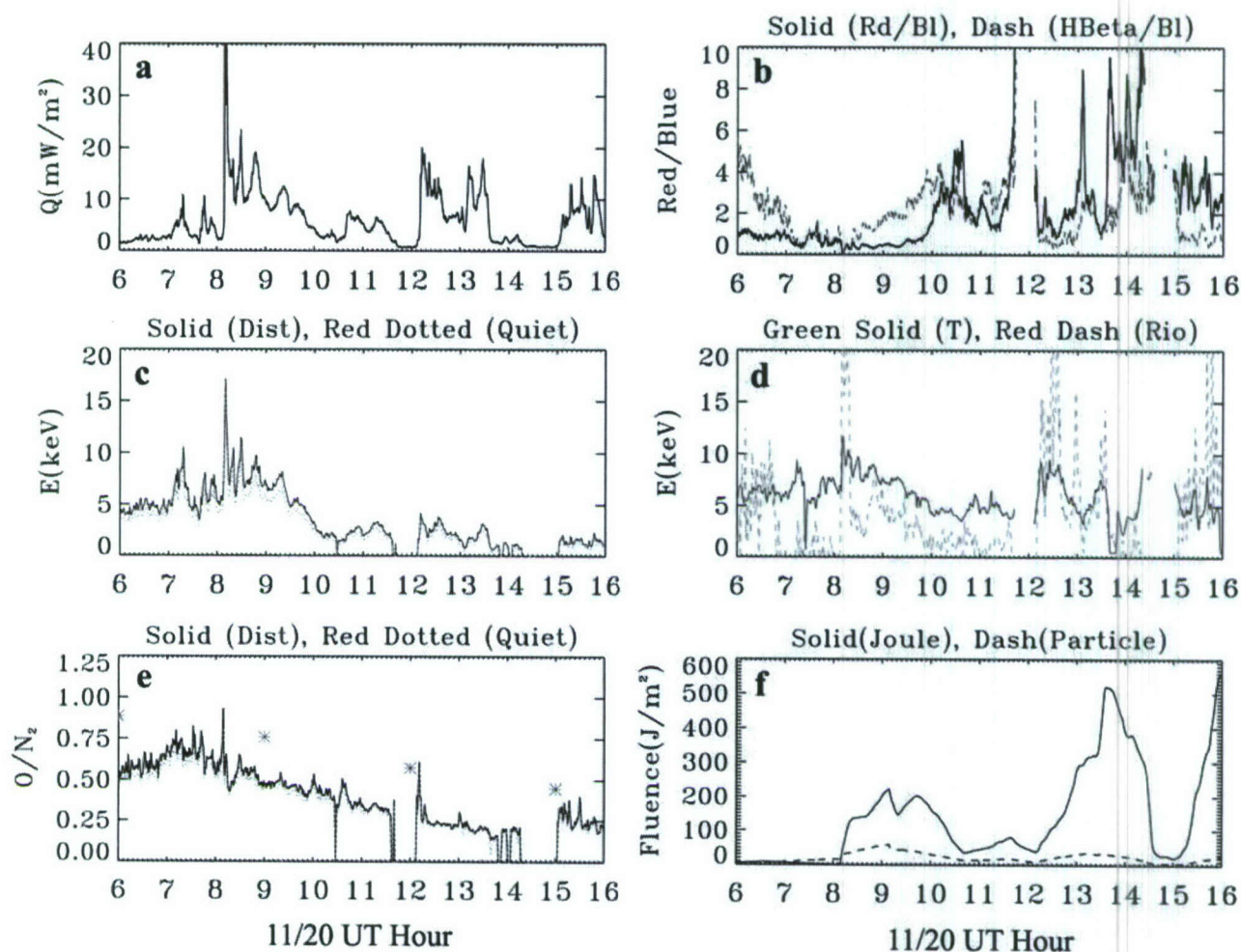
Figure 7. Same as Figure 4 except as noted. Plots of various quantities from DMSP F16 from the period of (a to g) 0400 to 2400 UT on 20 November 2003 and (aa to gg) 0000 to 1600 UT on 21 November 2003 during all times where Q(electron) is above 2 mW/m². The triangles and diamonds are described in Figure 4. Note that the scales for the same quantity are the same from day to day to visually enhance any differences especially with the results shown in Figure 4.

[87] There appear to be two regimes for the energetics on this night. Prior to 1000 UT (and including the period of large particle deposition around 0800 to 0900 UT) the red/blue ratio in Figure 8b is low, indicative of moderate to high values of E. These are consistent with those DMSP results which sample the nighttime auroral oval which for this period occurs in the southern hemisphere. Just before 1000 UT this ratio increases dramatically to values of 3 to 4 and it remains at that level or higher for the remainder of the night. The peak in the red/blue ratio is 15, although this peak occurs during a period of very low flux suggestive of

polar rain. However, at other times (e.g., 1300 UT) the increase in this ratio occurs coincident with a significant flux of particles. The absolute red intensity exceeds 10 kR during these times. These are all characteristics of great red aurorae [*Vallance Jones*, 1992].

[88] Figure 8b also shows the relative proton flux given by the ratio of H-Beta to blue, which has been scaled upward by a factor of 20 for clarity. Certainly proton precipitation is enhanced after 0800 UT through the rest of the night. However, there is no clear correlation with red/blue. There are periods when both increase, sugges-

Figure 8. Same as Figure 5 except where noted but for 20 November 2003. The "disturbed" atmosphere results are used. In Figure 8b the green line represents the ratio of H–Beta to blue from MSP data scaled upward by a factor of 20. In Figures 8c and 8e the red dotted line is for the "quiet" atmosphere.

tive of the presence of enhanced fluxes of low-energy electrons and protons. There are other periods where no such correlation exists. Note especially that the proton flux enhancement between 0800 and 1000 UT does not correlate with the changes in red/blue seen during that same period.
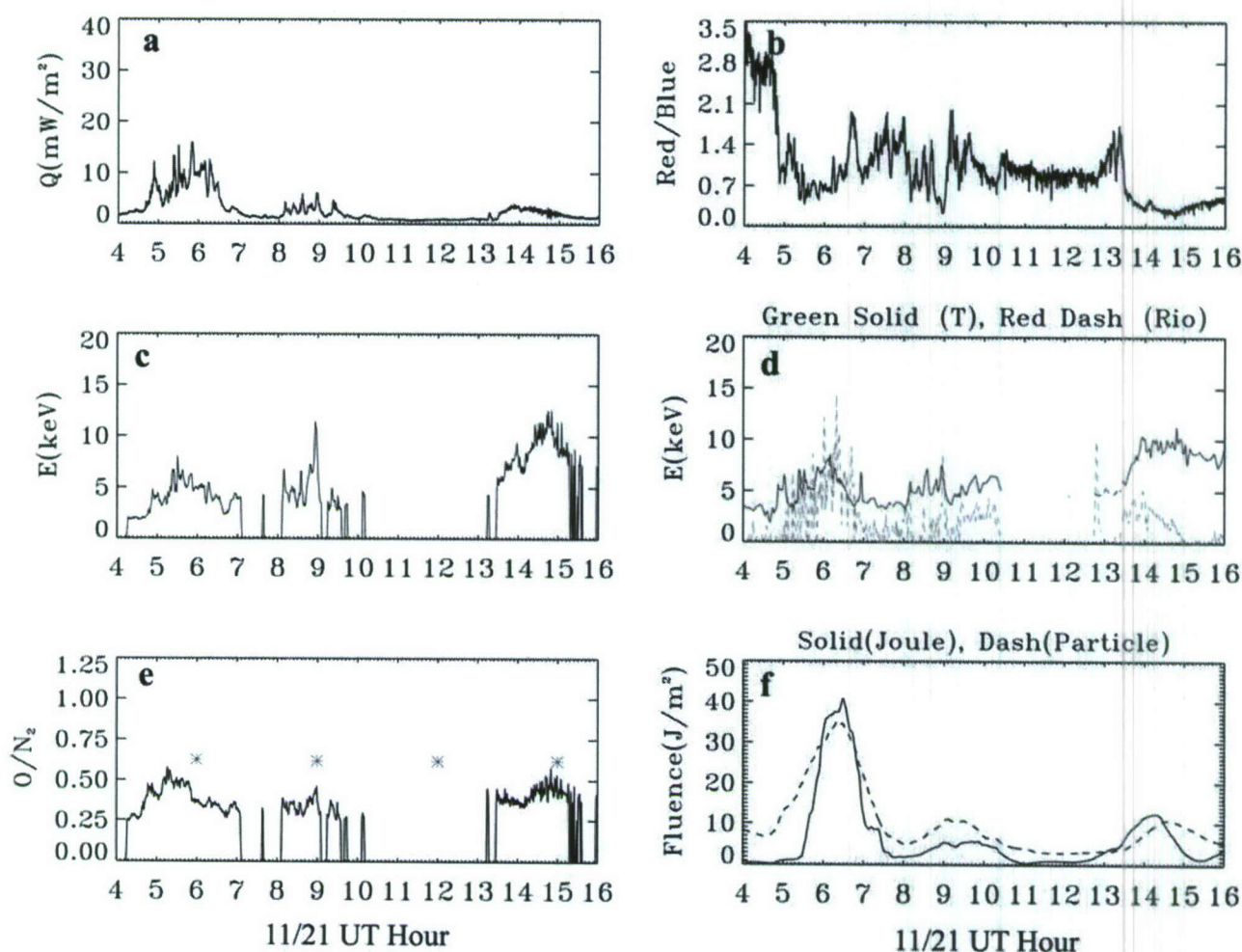
[89] The values of E derived from the three techniques (Figures 8c–8d) show some interesting trends. E derived from the red/blue versus OI (844.6 nm)/blue photometer technique (Figure 8c) shows values of 5 to 10 keV prior to 0930 UT, dropping to 1 to 2 keV after 1000 UT and the rest of the night. This seems consistent with the DMSP results. The temperature-derived E values shown in Figure 8d also show a decline, but not nearly as large with few values below 5 keV. This is not surprising because the temperature technique, as noted earlier, is relatively insensitive to the low-energy electrons, which would not strongly excite the green emission.

[90] Also plotted in Figure 8c are the E results derived using the "quiet" atmosphere. There are small differences with the energy(O/N$_2$) results in the quiet atmosphere being between about 10(5)% lower suggesting that the results

using the photometric technique are relatively independent of model atmosphere.

[91] The riometer-derived E values are also shown in Figure 8d. Since the riometer data are not sensitive to low-energy electrons, any such CNA should be interpreted as an indicator of high-energy electrons. Over a significant portion of the night, the riometer-derived E values are considerably lower, suggesting a relative absence of the high-energy electrons needed to produce CNA. Interestingly, in the period from 0600 to 0700 UT, high-energy electrons appear and then, just before the storm onset, this high-energy component disappears. Examination of all the imaging riometer pixels (not just those in the magnetic zenith) strongly suggest that because the enhancement in CNA prior to 0700 UT is an artifact, due to the passage of the radio star Cassiopeia-A. Ignoring the artifact, the period when high-energy electrons are present occurs almost impulsively around 0800 UT when the shock arrives. Some high-energy electrons remain after this event, but after 1000 UT they diminish considerably until ~1200 UT. The poor agreement between the riometer-derived E values

Figure 9. Same as Figure 8 but for 0400 to 1600 UT on 21 November 2003. The "disturbed" atmosphere results are used.

and the other techniques between 0700 and 0800 UT suggest an absence of very high-energy electrons during this period. The better agreement of the riometer-derived and temperature-derived E values after 1200 UT suggest the presence of a more nominal high-energy electron component.

[92] The O/N_2 results, which are derived from the photometer data, are shown in Figure 8e. Between 0600 and 0700 UT, Figure 8e shows values just above 0.6, a value slightly higher than was found at the end of 19 November. This value gradually increases to 0.75 and then decreases almost steadily until 1400 UT to about 0.2. It then increases to about 0.25 at 1600 UT. Also shown are the NRLMSIS values which start at about 0.9 at 0600 UT. These values decline to 0.75 at 0900 UT and continue to decline reaching a minimum of 0.45 at 15 UT. Similar to what was found for E, the results using the "quiet" atmosphere with the enhanced Gaussian are between 5 and 10 percent lower than when the "disturbed" atmosphere is used.

[93] There are several aspects of these results worth noting. First, the decline of the photometric-derived O/N_2 results is generally smooth. It does not show any jump at 1000 UT associated with the change in particle energetics. Second, NRLMSIS shows about a factor of two decrease
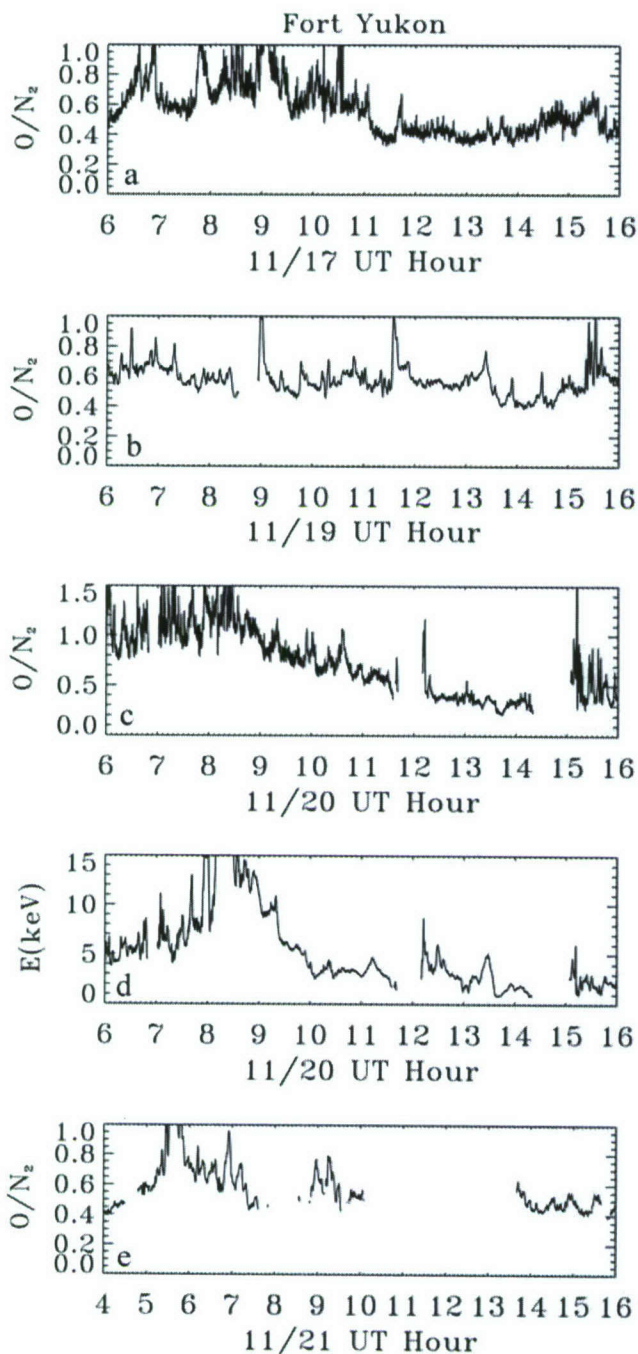
while the data show about a factor of 3 decrease. This is comparable to what was found during the great magnetic storm of February 1986 [*Hecht et al.*, 1991]. Third, these results are reassuring in that the composition results and the E values derived from the photometer technique (Figures 8c and 8e) are fairly insensitive to the choice of model atmosphere. Such a comparison was difficult to perform previously when the f_o scaling factor was used [*Hecht et al.*, 1991].

[94] Finally, Figure 8f shows F_J and F_P. Again F_J is significantly higher through most of the period. The F_J values, even when low (after 0800 UT), are generally much larger than on previous nights and are consistent with a continuous decline in O/N_2 seen throughout the night. The smallest F_J values (after 0800 UT) occur around 1500 UT and could be the reason for the slight increase in O/N_2 around that time. The electromagnetic energy fluence obtained by integrating Q_J over the 0000 to 1600 UT period is 2700 J/m², the largest value seen of all the observations reported on here and by *Hecht et al.* [2006].

3.3.2.2. Results for 21 November 2003
[95] Figure 9 shows the results for 21 November which covers the period after the peak of the storm. As seen in Figure 9a, only one large storm-related auroral event occurs

Figure 10. Plots of Fort Yukon photometer results. Except for Figure 10d, first point is at 0600 UT. (a) O/N_2 column density ratio on 17 November 2003. (b) Same as Figure 10a on 19 November 2003. (c) Same as Figure 10a on 20 November 2003. (d) E on 20 November 2003. (e) Same as Figure 10a on 21 November 2003.

with the photometer derived values in Figure 9c. The riometer-derived E values also shown in Figure 9d indicate an absence of high-energy particles prior to 0500 UT.

[96] The O/N_2 ratios both from the NRLMSIS model and from the data shown in Figure 9e are only slightly above those found on 20 November in the post-1000 UT period. The F_J values shown in Figure 9f are closer to that seen on 19 November than to the other nights. The total electromagnetic energy fluence for the night obtained from integrating Q_J from 0000 to 1600 UT is about 120 J/m^2, the lowest of the four nights presented here. Despite this small amount of heating, the O/N_2 ratios do not recover to their presuperstorm levels.

3.4. Other Data
3.4.1. Satellite Particle Data on 20–21 November
3.4.1.1. NOAA POES Data
[97] The POES data from NOAA-16 were shown in Figure 3 and discussed earlier. They show a marked increase in low-energy particles after 1000 UT until 2400 UT on 20 November. There is also a minimum in the low-energy component around 1600 UT consistent with the DMSP F16 data. On 21 November the data show increased low-energy particles between about 0200 and 0600 UT.

[98] The data for NOAA 17 (not shown) are similar to the NOAA-16 results. The only difference in these data is that the enhancement of the low-energy electrons after 2000 UT is larger than in the NOAA-16 results.

3.4.1.2. DMSP F15
[99] The data from the DMSP F15 J sensor also show an increase during 20 November in the very low energy (<0.1 keV) electrons but not to the same magnitude as was seen in F16. While the increase begins at 0800 UT, the fraction of the time these low-energy electrons are above 0.03 and thus carry more than 3 percent of the total flux, reaches a local maximum of around 0.1 at approximately 1030 UT. It stays around that value for the remainder of 20 November. There are some periods where this value (the fraction of time the low-energy particles carry more than 3 percent of the total flux) is higher, at almost 0.4, and lower, close to 0.01 near 1400 UT. However, in general this value is enhanced over the pre-0800 UT period, but below that seen in the F16 data. On 21 November (except for one orbit near 0200 UT that value is also enhanced in the F16 data) this value is at levels similar to the pre-0800 UT values on 20 November.
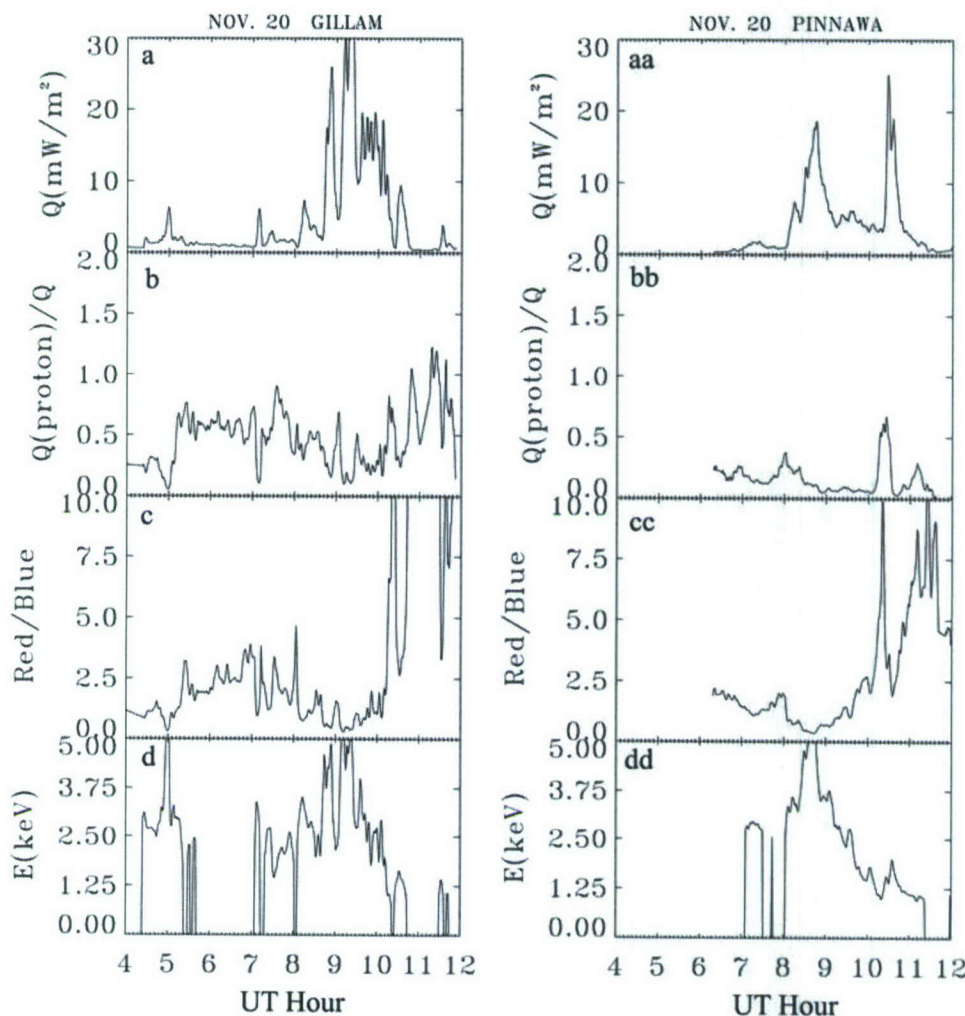
[100] The J sensor, however, does not appear to record the large flux seen on the ground in the Alaska data and on DMSP F16. This is probably because the pass through the auroral zone occurs near 0804 UT, which is before the large increase was recorded at Poker Flat.

3.4.2. Ground-Based Data
3.4.2.1. Fort Yukon Photometer
[101] Selected results from this instrument are shown for all four nights in Figure 10. The composition results shown in Figures 10a–10c and Figure 10e are similar to, but not identical with, those seen at Poker Flat. This is not surprising as the Joule heating, which appears to control most of this change, has a slightly different time history at the two sites. However, that the decrease in O/N_2 is largest on 20 November is confirmed by these data. Of particular

and that period is between 0500 and 0700 UT. During this time the red/blue ratio shown in Figure 9b is lower than on 20 November with values around 1 or less. The E values shown in Figure 9c are higher than on 20 November. Between 0400 and 0500 UT the red/blue ratio declines from values above 2 to less than 1. The temperature-derived E values shown in Figure 9d are in reasonable agreement

Figure 11. Plots of various quantities from (left) Gillam and (right) Pinnawa from meridian scanning photometer data during the period of 0000 to 1200 UT on 20 November 2003 where Q (particle) is above 1 mW/m^2, showing (a) Q(particle) derived from N$_2^+$ data, (b) Q(proton)/(Q(particle)), (c) red/blue, and (d) E derived using OI (557.7 nm)/blue versus red/blue using Figure 1c.

interest are the E data on 20 November shown in Figure 10d. As is found at Poker Flat, there is a significant decrease in E after about 0930 UT, and low values between 1 and 3 keV are measured throughout the rest of the night.

3.4.2.2. Pinnawa and Gillam Photometers

[102] To further investigate the large-scale nature of this low-energy particle precipitation, Figure 11 shows results from the two mid-Canadian photometer sites at Pinnawa and Gillam. Figures 11a and 11aa show the particle flux Q(particle) derived from the N$_2^+$ data. Also shown are the proton fraction (Figures 11b and 11bb), the red/blue ratio (Figures 11c and 11cc), and E (Figures 11d and 11dd).

[103] As is found at Poker Flat and at Fort Yukon, both Canadian sites show increases in red/blue and decreases in E after 0900 to 1000 UT. Around 0900 UT the E value is 5 keV, which decreases to close to 1 keV after 1000 UT. This is consistent with what was found at the two Alaska sites.
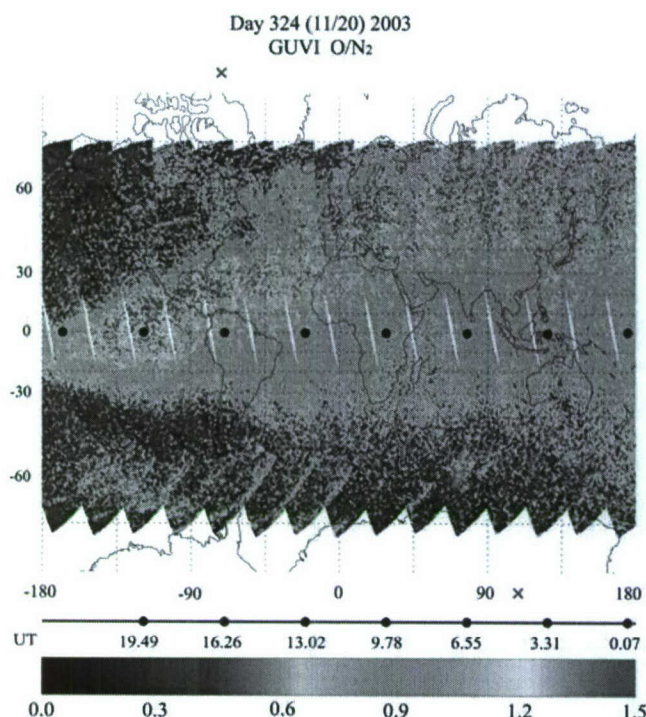
[104] One additional aspect of these data is also worth discussing. Figures 11b and 11bb show the ratio of the proton flux derived from H-beta, with the total flux derived

from the N$_2^+$ photometer. Both use constant values to convert the measured brightness to flux. In the case of the N$_2^+$ data these values are somewhat insensitive to E or to protons or electrons [*Strickland et al.*, 1993], as discussed earlier. However, the H-beta conversion is sensitive to the proton average energy and this uncertainty probably accounts for the values above 1 seen in Figure 11b.

3.4.3. GUVI Data

[105] As noted earlier, an extensive analysis of GUVI dayglow data has been reported for this period [*Meier et al.*, 2005; *Crowley et al.*, 2006]. Figure 12 shows the dayside O/N$_2$ column density ratio for 20 November. Although these orbits cover the entire 24 h UT period, the local solar time for the TIMED satellite during these dayside periods are generally between about 1000 and 1200 LST. (Specifically, a nominal southbound equatorial crossing occurs about 1150 LST. At 40N, 50N, and 60N these crossings occur around 1105, 1040, and 1000 LST, respectively.) Prior to 1000 UT the ratio has a value of about 1, consistent with geomagnetically quiet conditions. However, just after 1000 UT a large decrease in O/N$_2$ appears, propagating from the north toward the equator at

Day 324 (11/20) 2003
GUVI O/N₂

Figure 12. Dayside O/N_2 column ratio on 20 November 2003 derived from GUVI data. The two points marked as a red cross are the north and south magnetic poles. The mean UT times for equatorial crossings are shown on the black scale below.
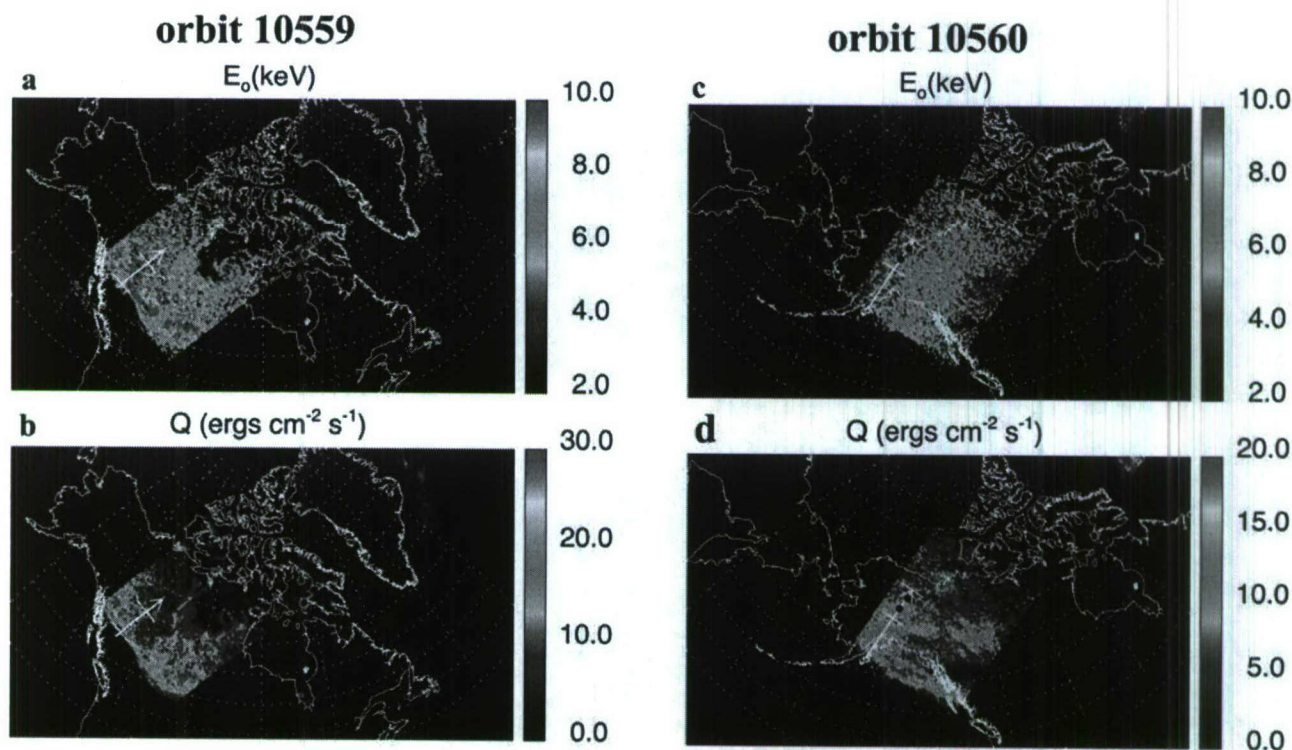
later UT. It is of interest to note that no such decrease is apparent in the period from 0800 to 1000 UT.

[106] Two orbits of nightside auroral zone GUVI data are most relevant to this study and these are shown in Figure 13. Figures 13a and 13b show plots of GUVI derived results for E and Q on 20 November from orbit 10559, which passes over Western Canada at about 0915 UT and from the next orbit which passes over Alaska around 1055 UT. The black dots in Figures 13c and 13d locate the Poker Flat and Fort Yukon ground sites. The white arrows show the satellite direction. The Q plots show the extent of the aurora which just reaches the US-Canadian border, a somewhat lower latitude than would be expected from the DMSP MABI. The E plots show a considerable reduction in E between these two orbits. This is qualitatively consistent with the other data sets. However, since the GUVI algorithm cannot reliably obtain average energies when they are below 2 keV, the magnitude of E more resembles that seen from the temperature-derived E values in Figure 8d. Unlike the single point photometer measurements, the GUVI data can be used to determine the geographical extent over which the low-energy particles were present.

4. Discussion
4.1. Composition Changes During This Storm Period

[107] Great magnetic storms are rare events and prior to this study, the only composition change data observed was during the 1986 storm [*Hecht et al.*, 1991]. The present storm is the first one since the four-channel photometric technique was adopted.

orbit 10559   orbit 10560

Figure 13. GUVI images of derived data on 20 November for two orbits, (left) 10559 at approximately 0915 UT and (right) 10560 at approximately 1055 UT. Shown is (a) E for 10559, (b) Q for 10559, (c) E for 10560, and (d) Q for 10560. The black dots in Figures 13c and 13d locate the Poker Flat and Fort Yukon sites. The white arrows, seen in the left corner of each swath, show the satellite direction.

4.1.1 Model Versus Data Comparison

[108] The NRLMSIS model results show small changes in O/N_2 during 19 November, slightly larger changes on 17 November, and the largest changes on 20 November. These trends follow the K_p and F_J values for these days. On 19 November the model shows that the O/N_2 values had recovered from the storm activity on 17 November. The model indicates a significant decline in the O/N_2 values on 20 November that only slightly recovered to prestorm values on 21 November.

[109] The data show a somewhat more dynamic picture. On 17 November, the absolute value of O/N_2 agreed with the model prior to the significant activity, but there was a much greater depletion in O/N_2 than seen by the model. On 19 November the inferred changes in O/N_2 are small and comparable to the model predictions although the absolute values are below the model. This suggests that recovery had not completely occurred from the prior day's geomagnetic activity. On 20 November both model and data show continuous decline during the night, although the data show a larger decrease of about a factor of three compared to the factor of two predicted by the model. The data on 21 November show that O/N2 had not recovered from the superstorm activity on 20 November, a result replicated by the model.

[110] Interestingly, the model seems to do a reasonable job of reproducing the changes in O/N_2 when there is little geomagnetic activity and during larger, more sustained events such as on 20 November. However, the model does a poorer job during moderate storms such as on 17 November. It appears as if the model, which uses 3 h a_p values, does not capture large geomagnetic effects on short timescales. Even during large storms such as on 20 November there is the tendency to underpredict the changes in O/N_2.

4.1.2. Causes of Composition Change

[111] As *Christensen et al.* [1997] have pointed out, the qualitative effects of auroral energy input have been known for a long time. Energy is deposited into the atmosphere due to dissipation of electric currents, known as Joule heating, and due to the dissipation of kinetic energy from precipitating particles. These energy losses cause circulation cells to form, vertical winds to increase in the vicinity of the heating, and subsequent uplifting of air parcels containing relatively little atomic oxygen. At a given altitude above the heating this results in a reduction of the ratio of light molecular weight species to heavy molecular weight species [e.g., *Hays et al.*, 1973; *Prölss*, 1980]. Certainly, for large geomagnetic storms and at altitudes above 150 km, such effects are found in the predictions of the MSIS models. Similar effects should also be seen on a more local scale during and after auroral substorms. Thus deposition of auroral energy should drive vertical circulation, resulting in changes in atmospheric composition. What is not known is how well current models reproduce actual composition change during auroral activity.

[112] On the 3 d with significant declines in O/N_2 during the night, F_J greatly exceeds F_P. Thus it appears that one major cause of changes in O/N_2 is the magnitude of F_J. Clearly transport effects may also be important [*Hecht et al.*, 2000] and that may be partly responsible for the low O/N_2 values on 21 November and on 19 November, but more

work needs to be done to quantify the importance of transport.

4.2. Magnetic Cloud and Low-Energy Particles

[113] *Sivjee and Shen* [1997] proposed that the precipitation of low-energy particles whose average energies are considerably below 1 keV may be associated with the passage of magnetic clouds. Those results were based on temperatures inferred from optical emissions observed over Kangerlussuaq, Greenland (67N, 209E geographic, 74.5N, 41.6W geomagnetic). Like the present observations, that event occurred during a major magnetic storm in which Dst reached −130 nT. The new data presented for the storm on 20 November 2003 support the thesis of *Sivjee and Shen* [1997] that there is an enhancement of low-energy particles during a magnetic cloud event.

[114] The plasma properties in the solar wind can be determined from spacecraft data. *Gopalswamy et al.* [2005b] notes that the initial solar wind shock was present at L1 around 0728 UT. Allowing approximately 0.7 h to advance the shock from L1 to the magnetopause, the period just after 0810 UT should correspond to observations of enhanced auroral electron flux. This is indeed what was seen by the ground-based photometers at Poker Flat at 0810 UT and the DMSP F16 J sensor around 0813 UT. However, the F15 J sensor that passed through the auroral zone around 0804 UT did not see an enhanced auroral electron flux since that probably occurred before the shock reached the magnetopause.

[115] *Gopalswamy et al.* [2005b] discusses a magnetic cloud associated with an interplanetary coronal mass ejection (ICME) that was present around the Earth starting at approximately 1000 to 1100 UT on 20 November 2003 and ending around 0000 UT on 21 November 2003. The passage of the cloud was marked by enhanced, smoothly rotating magnetic fields, enhanced proton density, and a greatly depressed plasma β, which is the ratio of the bulk plasma thermal pressure to the magnetic field pressure, relative to the ambient solar wind [*Gopalswamy et al.*, 2005b, Figure 1]. These three features characterize magnetic clouds [*Burlaga*, 1991].

[116] Although the magnetic cloud comprised most of the disturbed interval inside the ICME, there were two additional periods of enhanced proton density and reduced plasma β. The first occurred at the end of the sheath region between the shock and the cloud where, between 0900 and 1000 UT, the plasma β is sharply reduced. The second is following the cloud and extends from approximately 0000 UT to 0600 UT on 21 November 2003. Although the plasma β remains below 1 throughout this interval, it should be noted that this period is associated with an enhancement in the plasma β compared to the magnetic cloud interval. H-alpha images from SOHO during the solar event show a dense filamentary structure ejected along with the CME. The subsequent observation of the enhanced density region in the ACE data is consistent with such filamentary material, which is often found in the trailing edge of ICMEs [*Gopalswamy et al.*, 1998].

[117] As noted above most of the data presented in this paper support the assertion by *Sivjee and Shen* [1997] that the precipitation of lower average energy particles may be associated with magnetic clouds. The ground-based data

from both Alaska and Canadian sites show a decrease in E in the period from 0900 to 1000 UT. This decrease in E persists through the rest of 20 November. The Alaska data show low E values until about 0400 UT on 21 November, after which they begin to increase. Taken alone, these data would suggest that lower E values are associated in some way with the passage of the core of the magnetic cloud occurring from 1000 to 2400 UT on 20 November. However, looking at the boundary regions of the cloud, the data suggest a much sharper boundary for the low-energy particles associated with the front of the cloud and a more diffuse boundary on the backside of the cloud. The NOAA data from Figure 3b, which show a persistent enhanced low-energy electron flux component during the passage of the magnetic cloud, also support this picture.

[118] The DMSP J data and the red/blue data, however, suggest that this picture is incomplete. The enhancement of the red/blue, although an indicator of a lower E value, may also be indicative of enhanced precipitation of soft electrons with energies of a few hundred eV or less, which are the cause of Type A red aurora. In fact, the F16 J sensor data clearly show that besides a lowering of E there is also an enhancement in the low-energy electrons below 0.1 keV. This enhancement occurs from about 1000 UT until 2400 UT encompassing the period of the magnetic cloud. The F15 J sensor data are also consistent with this picture of enhanced low-energy particle precipitation associated with the magnetic cloud, although these data do not show the same enhancement as is seen in the F16 orbit.

[119] Overall, the data show the enhanced precipitation of low-energy flux coincides with the passage of the magnetic cloud. This is consistent with the assertion by *Sivjee and Shen* [1997] that interactions of magnetic clouds with the magnetosphere may trigger the precipitation of low-energy particles which are the cause of Type A red aurora. While our current observations provide considerable evidence that there is a connection between the passage of the magnetic cloud and enhanced low-energy electron precipitation, we agree with *Steele et al.* [1998] that questions regarding the exact source of such particles during magnetic cloud events require a further detailed study of the magnetospheric data.

4.2.1. Shape of the Energy Distribution

[120] Throughout the paper, it has been assumed that Gaussians are primarily responsible for the observed auroral emission. In many previous studies, radar data had been available that showed that even during superstorms a Gaussian was the predominant shape of the energy distribution [e.g., *Hecht et al.*, 1991]. However, here no such data exists and so we now show the changes that occur in the derived quantities if Maxwellians were assumed.

[121] Figure 14 shows plots of the E and O/N_2 quantities assuming either a Maxwellian with a low-energy tail or the enhanced Gaussians used above, both of which are based on *Strickland et al.* [1993]. The left column shows the time series plots for these derived quantities for two nights 19 November and 20 November. The right column shows the percent differences. On 19 November (Figure 14a–14d) the results show that on average the derived E and O/N_2 quantities are higher on average by 10–15 and 20–30%, respectively. Since none of the results of this paper are affected by such an uncertainty in E, this suggests that the exact nature of the distribution is not so significant.

However, the same cannot be said for O/N_2. While on 17 November the essential conclusions that are based on O/N_2 are not affected by this uncertainty, on 19 November the relatively small magnitude of the change during the Joule heating event could be affected. This is especially so as one could argue that there is no decrease in O/N_2, but only a change in the shape of the distribution.

[122] Figures 14e–14h show the results for 20 November. Here it is seen that, although there are periods where the changes may be larger (or smaller) than the nominal numbers quoted above, they would not affect our conclusions. If Maxwellians occurred, say, prior to 1000 UT, this would result in a larger E and O/N_2. The larger O/N_2 would thus indicate an even larger decrease than predicted by the model over the night. After 1000 UT the choice of distribution has much less of an effect rendering the choice of distribution unimportant as to which is used in the analysis.

[123] Nevertheless, there is a method in which the optical data can be used to determine whether the auroral emissions are being caused by Gaussians or Maxwellians. It had long been noted that Q and E were often positively correlated. *Christensen et al.* [1987] first showed that this was a consequence of the presence of Gaussian electron distributions. They showed that the relationship between Q and E should be related by the following when the electrons are accelerated down a field line producing a Gaussians energy distribution
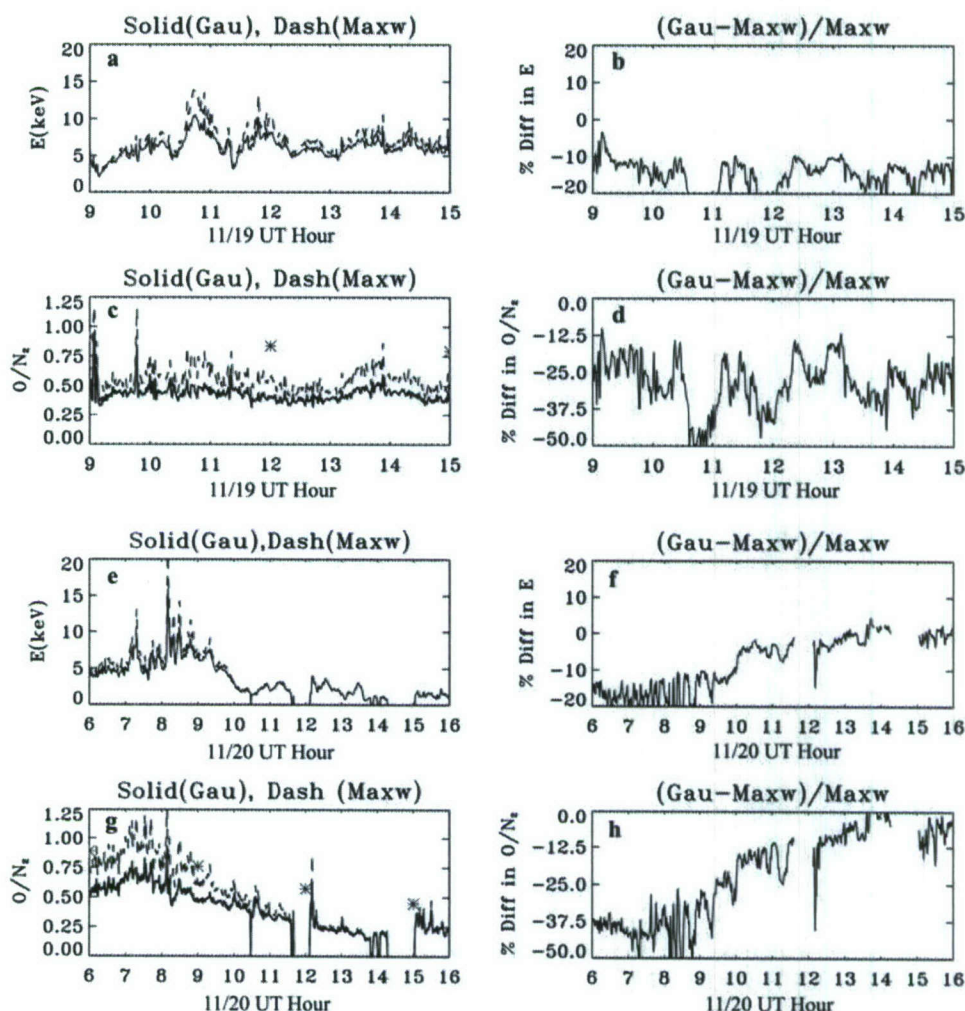
$$Q = kE^g \tag{1}$$

where g should typically be between 1.5 and 2 for most acceleration conditions depending mainly on the magnetic field strengths in the magnetosphere and ionosphere [*Christensen et al.*, 1987]. The constant k is linearly related to the product of the plasma density in the plasma source region and the square root of the thermal energy. *Strickland et al.* [1994] validated this using radar data and showed that Gaussian distributions indeed showed such a correlation although the g values might be somewhat lower and higher probably because the plasma conditions were changing during the observation period. When Maxwellians were present no correlations were seen. Thus this technique allows the determination of not only the type of energy distribution but also allows some insight into the conditions in the plasma source region.

[124] Figure 15 and Table 3 shows the results for three of the nights in this study, 17 November, 19 November, and 20 November. The left column of Figure 15 shows the time series plots of Q and E. Since the E values are not affected much by any prior knowledge of the distribution, the Gaussian results were used. It is easy to see visually that for most periods the Q and E values appear correlated. To quantify this, the right column shows the scatter plots of E versus Q, while Table 3 shows the results for k and g. For each night at least one blue line is shown that shows the fit obtained by using the fitted k and g parameters. Most of the data do appear correlated with g values consistent with what was found by *Strickland et al.* [1994] confirming that Gaussian distributions are appropriate. The following is a brief discussion of each night.

[125] On 17 November the data from the two substorms were combined and shown as the black data in Figure 15b.

Figure 14. (left) Plots of Q and E derived from red/blue versus 844.6 nm/blue technique at Poker Flat for 19 November and 20 November. These are derived using the enhanced Gaussians (solid black line) and Maxwellians (dashed green line). Also shown are (right) percent differences. Shown are (a) 19 November E, (b) 19 November percent difference for E, (c) 19 November O/N$_2$, (d) 19 November percent difference for O/N$_2$, (e) 20 November E, (f) 20 November percent difference for E, (g) 20 November O/N$_2$, and (h) 20 November percent difference for O/N$_2$.

The g value is quite similar to the *Strickland et al.* [1994] results. They did not report k values though. The green and red data are for the period between the substorms. These do appear appear to be well correlated. Thus Maxwellians might be appropriate here. However, on the basis of Figure 5 this would not change any of the conclusions we find with respect to the observed versus modelled O/N$_2$ variations.
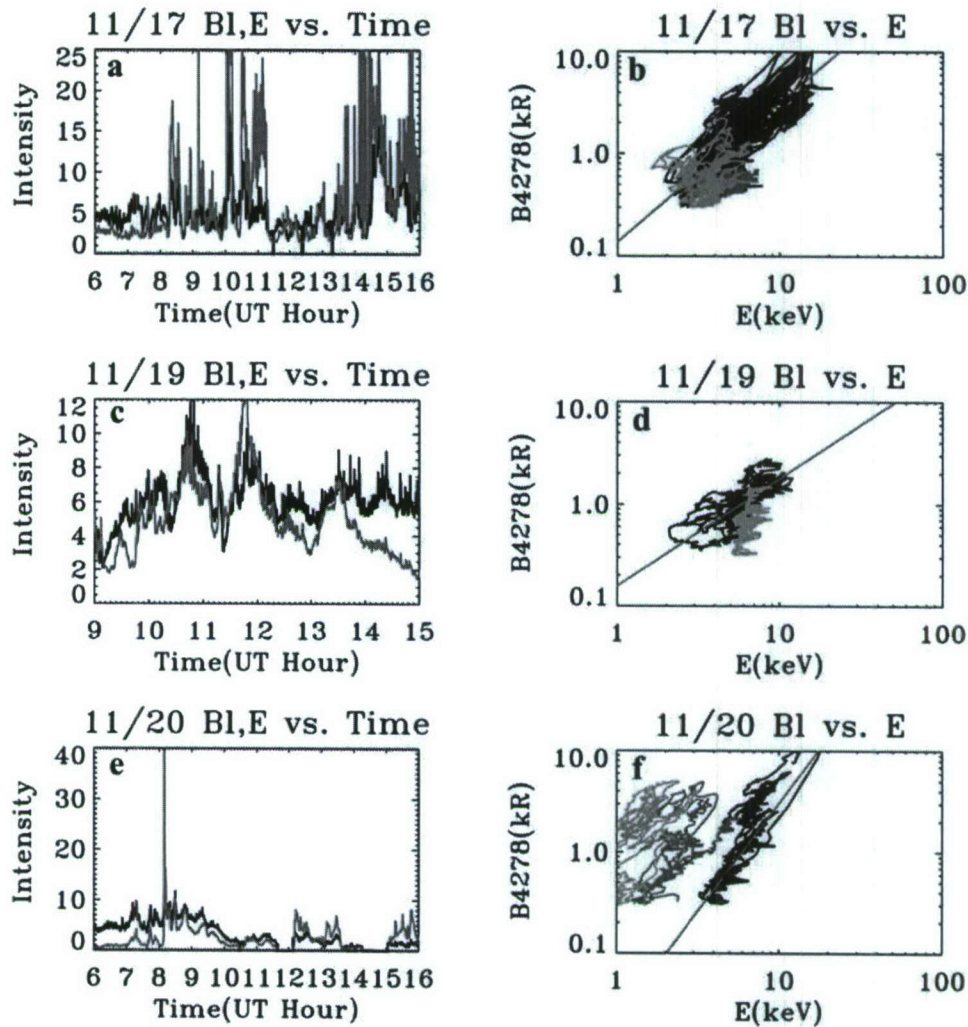
[126] On 19 November where the observed variations in O/N$_2$ were small Gaussians are appropriate during the observing period where the O/N$_2$ variations occurred. Maxwelllians might be appropriate at the end of the observing period. The latter is where postmidnight diffuse aurora can occur [*Hecht et al.*, 1995]. Again a 25% increase in O/N$_2$ during the period from 1330 to 1500 UT would not affect our conclusions.

[127] The results from 20 November, though, are the most interesting. The analysis shown in Figure 14 indicated that a knowledge of the type of energy distribution in the period before 1000 UT would have a much larger affect on

the O/N$_2$ results than during later times. In fact almost all the data on this night appear correlated and consistent with Gaussians. Note that during the great magnetic storm of 1986 Gaussians were almost always observed [*Hecht et al.*, 1991].

[128] Unlike the other nights where the scatterplots show the data are clustered, on 20 November the data undergo many transitions as shown in Figure 15f and in Table 3. This is reflected by variations of g, which are associated with magnetic field strengths in the magentosphere and ionosphere, and, more interestingly, by variations in k which are related to changes in the plasma source region. From 0600 to 0800 UT before the ICME shock hits the magnetosphere, k is quite low. These data are shown in black and the blue fit is plotted through this data set. After the shock hits, another cluster of black data are shown but these are shifted to the left. The slope is quite similar but k has increased by somewhat less than a factor of 2. This transition occurs just after the shock. The next data set, shown in green, represents the period from 930 to 1030 UT,

Figure 15. (left) Plots of the Blue intensity in kR (green line) and E in keV (black line) derived from red/blue versus OI(844.6 nm)/blue photometric technique at Poker Flat for 17 November, 19 November, and 20 November. The Q and E values are the same as are shown in Figures 6a, 6c, 8a, and 8c. These are derived using the enhanced Gaussians. Also shown are (right) these *E* versus Q scatterplots. In the scatterplots, different time intervals are represented by different colors mostly indicated in the title. In each plot at least one blue line is shown which is the best linear fit to the selected color group. Shown are (a) 17 November Q and E plots and (b) 17 November scatterplot, with black representing 0800 to 1130 and 1330 to 1600 UT, green representing 0600 to 0800 UT, and red representing 1130 to 1330 UT. Blue line is a fit to the black data. Also shown are (c) 19 November Q and E plots and (d) 19 November scatterplot, with black representing 0900 to 1330 UT and red representing 1330 to 1500 UT. Blue line is a fit to the black data. Finally, shown are (e) 20 November Q and E plots and (f) 20 November scatter plot, with black representing 0600 to 0800 UT (Blue line is a fit to the black data.), black data to the upper left representing 0800 to 0930 UT, green data representing 0930 to 1030 UT, blue data representing 1030 to 1330 UT, red representing 1330 to 1515 UT, and light green data representing 1515 to 1600 UT.

the transition period through which the magnetic cloud is encountering the Earth's magnetosphere. During this period, the k value undergoes a large increase. However, these data still appear to be connected to the 0800–0930 UT data and the variations in k and g could be due to changing conditions in the plasma source region. The subsequent data after 1030 UT, shown in blue, red, and light green, clearly have a different character than any of the data seen on the previous nights. If these data are simply interpreted in terms of the *Christensen et al.* [1987] analysis then the k values have increased by almost two orders of magnitude.

Perhaps other processes are occurring since, as *Christensen et al.* [1987] note, their analysis does not apply to downward field-aligned currents. Nevertheless, these results clearly support our thesis that the magnetic cloud period is distinctly different than the periods of auroral activity that occurred on previous nights.

5. Conclusions

[129] In the introduction five questions were introduced whose answers are now presented:

Table 3. Results of Fit to Function $Q = kE^g$ for November 2003 Storm Period

Day	UT Hour Range	k	g	Plot Color	Notes
17	0800–1130, 1330–1600	0.14	1.36	black	two substorms
19	0600–0800, 1130–1330	0.16	1.05	black	two substorms
20	0600–0800	0.022	2.14	black(blue line fit)	prior to ICME shock
20	0800–0930	0.036	2.23	black	after shock before magnetic cloud
20	0930–1030	0.22	1.32	dark green	transition to magnetic cloud
20	1030–1300	0.27	1.77	blue	magnetic cloud
20	1300–1515	0.56	1.79	red	magnetic cloud
20	1515–1600	1.61	1.18	light green(below 2 keV)	magnetic cloud

[130] 1. Are the energy distributions of the electron precipitation different during the superstorm that began about 0800 UT on 20 November and continued through the first few hours of 21 November, than before the storm?

[131] Yes, although there are two caveats. First, the ground-based data at Poker indicate, on the basis of the good correlation between Q and E, that most of the time an enhanced Gaussian distribution was appropriate, rather than a Maxwellian, to represent the electron energy distribution for the model analysis. Second, prior to 1000 UT on 20 November the E values seen from both the satellite and ground-based data were consistent with those seen on most prior days including those seen on 19 November, the geomagnetically quietest day of this period. However, after 1000 UT on 20 November and continuing until the first few hours of 21 November the E values are lower than during other periods, including the period of enhanced auroral activity seen on 17 November. The low E values are obtained at the ground-based sites in Alaska and Canada and also in most of the DMSP and POES satellite data. While occasionally some of the satellite data showed low E values on 17 November and 19 November, the period from about 1000 to 2400 UT on 20 November, unlike any other period, had electron energy distributions characterized by a large enhancement in the flux below 0.1 keV. The early hours of 21 November showed some enhancement in this low-energy flux but much reduced from that seen on 20 November.

[132] 2. Is there a connection between the passage of the magnetic cloud during this storm and the low-energy particle precipitation as suggested by *Sivjee and Shen* [1997] from earlier observations?

[133] Although the 20 November superstorm was initiated by the passage of a solar wind shock by the Earth near 0800 UT, a decrease in the average electron energy or a large enhancement in low-energy particles was not associated with the shock. A large enhancement in the very low energy electrons was observed by the DMSP F16 J sensor during the period of 1000 to 2400 UT on 20 November, which corresponds to the time of the passage of the magnetic cloud as defined by *Gopalswamy et al.* [2005b]. Some lesser enhancements compared to the previous nights were seen just before and after the period of the cloud suggesting the cloud boundary may not be sharp. In addition, during the magnetic cloud passage, large red/blue ratios were seen suggestive of the presence of Type A red aurora. Thus taken together these support the assertion by *Sivjee and Shen* [1997] that the interaction of the magnetic cloud with the magnetosphere may trigger an enhancement of low-energy electron precipitation responsible for such aurorae.

[134] Nevertheless, the exact connection between such precipitation, the passage of the magnetic cloud, and any delayed effects of the large shock that occurred about 0800 UT need to be further investigated. To date, the connection between low-energy particles and magnetic clouds rests on only the example in this paper and the previous few studies by *Sivjee and Shen* [1997] and *Steele et al.* [1998]. In this work we have shown using the measured relationships between Q and E that the period after 1000 UT on 20 November is distinctly different than what was seen prior to that period. In the context of the *Christensen et al.* [1987] analysis this might mean changes in the plasma source region, or perhaps, different processes are occurring than the electric field acceleration considered in that work.

[135] 3. To what extent do the O/N_2 model (NRLMSIS) predictions and actual observations agree during the period before and during the superstorm?

[136] Although NRLMSIS predicted changes in O/N_2 generally follow K_p because of its 3 h timescale, the model does not fully capture composition changes due to geomagnetic activity. During the low geomagnetic activity night of 19 November the model and data results are similar reflecting the small changes that occurred that night. On the superstorm night of 20 November the model captures the general trend of decreasing O/N_2 during the night but underpredicts the magnitude. The data show a factor of three decrease in O/N_2, which is comparable to what was found during the 1986 superstorm discussed by *Hecht et al.* [1991]. However, the largest difference is on 17 November where the model and data show large differences during the time of peak fluence F_J. This difference is most likely related to the shorter time duration of the Joule heating on this night compared to the sustained periods of intense Joule heating on 20 November.

[137] 4. In particular, do we see any difference in O/N_2 between the model and observations during the time period of the magnetic cloud event?

[138] No. The magnetic cloud period does not show any particular increase in the rate of decline of O/N_2. The only interesting aspect is that the dayside decrease in O/N_2 reported by GUVI appears to begin at the time of the passage of the magnetic cloud.

[139] 5. Do any of the observed atmospheric composition changes correspond to inputs of auroral Joule or particle energy into the thermosphere?

[140] Yes. The decreases in O/N_2 appear to scale with the energy input into the atmosphere over periods of an hour or more. The largest decreases in O/N_2 occur during periods when F_J peaks. F_J especially exceeds the fluence due to auroral particles on 20 November. This is similar to what

has been previously reported and is summarized by *Hecht et al.* [2006].

References

Burlaga, L. F. (1991), Magnetic clouds, in *Physics of the Inner Heliosphere*, vol. II, edited by R. Schwenn and E. Marsch, pp. 1–22, Springer, New York.
Christensen, A. B., L. R. Lyons, J. H. Hecht, G. G. Sivjee, R. R. Meier, and D. J. Strickland (1987), Magnetic field-aligned electric field acceleration and the characteristics of the optical aurora, *J. Geophys. Res.*, 92, 6163–6167.
Christensen, A. B., J. H. Hecht, R. L. Walterscheid, M. F. Larsen, and W. E. Sharp (1997), Depletion of oxygen in aurora: Evidence for a local mechanism, *J. Geophys. Res.*, 102, 22,273–22,277.
Christensen, A. B., et al. (2003), Initial observations with the Global Ultraviolet Imager (GUVI) in the NASA TIMED satellite mission, *J. Geophys. Res.*, 108(A12), 1451, doi:10.1029/2003JA009918.
Conde, M., and R. W. Smith (1998), Spatial structure in the thermospheric horizontal wind above Poker Flat, Alaska, during solar minimum, *J. Geophys. Res.*, 103, 9449–9472.
Coumans, V., J.-C. Gerarad, B. Hubert, and D. S. Evans (2002), Electron and proton excitation of the FUV aurorae: Simultaneous IMAGE and NOAA observations, *J. Geophys. Res.*, 107(A11), 1347, doi:10.1029/2001JA009233.
Crowley, G., et al. (2006), Global thermosphere-ionosphere response to onset of November 20, 2003 magnetic storm, *J. Geophys. Res.*, 111, A10S18, doi:10.1029/2005JA011518.
Duboin, M., and Y. Kamide (1984), Latitudinal variations of Joule heating due to the auroral electrojets, *J. Geophys. Res.*, 89, 245–251.
Evans, D. S., and M. G. Greer (2004), Polar Orbiting Environmental Satellite Space Environment Monitor-2: Instrument descriptions and archive data documentation, *NOAA Tech. Memo. 1.4*, Space Environ. Cent., Boulder, Colo.
Gattinger, R. L., A. V. Jones, J. H. Hecht, D. J. Strickland, and J. Kelly (1991), Comparison of ground-based optical observations of N2 second positive to N2+ first negative emission ratios with electron precipitation energies inferred from the Sondre Stromfjord radar, *J. Geophys. Res.*, 96, 11,341–11,352.
Gopalswamy, N., et al. (1998), On the relationship between coronal mass ejections and magnetic clouds, *Geophys. Res. Lett.*, 25, 2485–2488.
Gopalswamy, N., L. Barbieri, E. W. Cliver, G. Lu, S. P. Plunkett, and R. M. Skoug (2005a), Introduction to violent Sun-Earth connection events of October–November 2003, *J. Geophys. Res.*, 110, A09S00, doi:10.1029/2005JA011268.
Gopalswamy, N., S. Yashiro, G. Michalek, H. Xie, R. P. Lepping, and R. A. Howard (2005b), Solar source of the largest geomagnetic storm of cycle 23, *Geophys. Res. Lett.*, 32, L12S09, doi:10.1029/2004GL021639.
Gosling, J. T. (1997), Coronal mass ejections: An overview, in *Coronal Mass Ejections, Geophys. Monogr. Ser.*, vol. 99, edited by N. Crooker, J. A. Joselyn, and J. Feynman, pp. 9–16, AGU, Washington, D. C.
Hays, P. B., R. A. Jones, and M. H. Rees (1973), Auroral heating and the composition of the neutral atmosphere, *Planet. Space Sci.*, 21, 559–573.
Hecht, J. H., A. B. Christensen, D. J. Strickland, and R. R. Meier (1989), Deducing composition and incident electron spectra from ground-based auroral optical measurements: Variations in oxygen density, *J. Geophys. Res.*, 94, 13,553–13,563.

Hecht, J. H., D. J. Strickland, A. B. Christensen, D. C. Kayser, and R. L. Walterscheid (1991), Lower thermospheric composition changes derived from optical and radar data taken at Sondre Stromfjord during the great magnetic storm of February 1986, *J. Geophys. Res.*, 96, 5757–5776.
Hecht, J. H., A. B. Christensen, D. J. Gutierrez, W. E. Sharp, J. R. Sharber, J. D. Winningham, R. A. Frahm, D. J. Strickland, and D. J. McEwen (1995), Observations of the neutral atmosphere between 100 to 200 km using ARIA rocketborne and ground-based instruments, *J. Geophys. Res.*, 100, 17,285–17,298.
Hecht, J. H., A. B. Christensen, D. J. Strickland, T. Majeed, R. L. Gattinger, and A. Vallance Jones (1999), Comparison between auroral particle characteristics and atmospheric composition inferred from analyzing optical emission measurements alone and in combination with incoherent scatter radar measurements, *J. Geophys. Res.*, 104, 33–44.
Hecht, J. H., D. L. McKenzie, A. B. Christensen, D. J. Strickland, J. P. Thayer, and J. Watermann (2000), Simultaneous observations of lower thermospheric composition change during moderate auroral activity from Kangerlussuaq and Narsarsuaq, Greenland, *J. Geophys. Res.*, 105, 27,109–27,118.
Hecht, J. H., D. J. Strickland, and M. G. Conde (2006), The application of ground-based optical techniques for inferring electron energy deposition and composition change during auroral precipitation events, *J. Atmos. Sol. Terr. Phys.*, 68, 1502–1519.
Hedin, A. E. (1983), A revised thermospheric model based on mass spectrometer and incoherent scatter radar data: MSIS-83, *J. Geophys. Res.*, 88, 10,170–10,188.
Hedin, A. E. (1991), Extension of the MSIS thermosphere model into the middle and lower atmosphere, *J. Geophys. Res.*, 96, 1159–1172.
Kayser, D. C., and W. E. Potter (1976), Molecular oxygen measurements at 200 km from AE-D near winter solstice, *Geophys. Res. Lett.*, 3, 455–458.
Kosch, M. J., F. Honary, C. F. del Pozo, S. R. Marple, and T. Hagfors (2001), High-resolution maps of the characteristic energy of precipitating auroral particles, *J. Geophys. Res.*, 106, 28,925–28,938.
Lummerzheim, D., M. H. Rees, and G. J. Romick (1990), The application of spectroscopic studies of the aurora to thermospheric neutral composition, *Planet. Space Sci.*, 38, 67–78.
Meier, R., G. Crowley, D. J. Strickland, A. B. Christensen, L. J. Paxton, D. Morrison, and C. L. Hackert (2005), First look at the 20 November 2003 superstorm with TIMED/GUVI: Comparisons with a thermospheric global circulation model, *J. Geophys. Res.*, 110, A09S41, doi:10.1029/2004JA010990.
Mori, H., M. Ishii, Y. Murayama, M. Kubota, K. Sakanoi, M.-Y. Yamamoto, Y. Monzen, D. Lummerzheim, and B. J. Watkins (2004), Energy distribution of precipitating electrons estimated from optical and cosmic noise absorption measurements, *Ann. Geophys.*, 22, 1613–1622.
Mulligan, T., and C. T. Russell (2001), Multispacecraft modeling of the flux rope structure of interplanetary coronal mass ejections: Cylindrically symmetric versus nonsymmetric topologies, *J. Geophys. Res.*, 106, 10,581–10,596.
Murayama, Y., H. Mori, S. Kainuma, M. Ishii, I. Nishimuta, K. Igarashi, H. Yamagishi, and M. Nishino (1997), Development of a high-resolution imaging riometer for the middle and upper atmosphere observation program at Poker Flat, Alaska, *J. Atmos. Terr. Phys.*, 59, 925–937.
Niciejewski, R. J., et al. (1989), Coordinated satellite and ground-based measurements of the energy characteristics of a Sun-aligned arc over Sondre Stromfjord, *J. Geophys. Res.*, 94, 17,201–17,213.
Nicholas, A. C., J. D. Craven, and L. A. Frank (1997), A survey of large-scale variations in thermospheric oxygen column density with magnetic activity as inferred from observations of the FUV dayglow, *J. Geophys. Res.*, 102, 4493–4510.
Nier, A. O., W. E. Potter, and D. C. Kayser (1976), Atomic and molecular oxygen densities in the lower thermosphere, *J. Geophys. Res.*, 81, 17–24.
Picone, J. M., A. E. Hedin, D. P. Drob, and A. C. Aikin (2002), NRLMSISE-00 empirical model of the atmosphere: Statistical comparisons and scientific issues, *J. Geophys. Res.*, 107(A12), 1468, doi:10.1029/2002JA009430.
Prölss, G. W. (1980), Magnetic storm associated perturbations of the upper atmosphere: Recent results obtained by satellite-borne gas analyzers, *Rev. Geophys.*, 18, 183–202.
Rich, F. J., and W. F. Denig (1992), The major magnetic storm of March 13–14, 1989 and associated ionospheric effects, *Can. J. Phys.*, 70, 510–525.
Richmond, A. D. (1995), Ionospheric electrodynamics using magnetic apex coordinates, *J. Geomagn. Geoelectr.*, 47, 191–212.
Robinson, R. M., S. B. Mende, R. R. Vondrak, J. U. Kozyra, and A. F. Nagy (1985), Radar and photometric measurements of an intense type A red aurora, *J. Geophys. Res.*, 90, 457–466.
Sivjee, G. G., and D. Shen (1997), Auroral optical emissions during the solar magnetic cloud event of October 1995, *J. Geophys. Res.*, 102, 7431–7438.

Steele, D. P., D. J. McEwen, and G. G. Sivjee (1998), Ground-based optical observations from the north magnetic pole during the January 1997 magnetic cloud event, *Geophys. Res. Lett.*, *25*, 2573–2576.

Strickland, D. J., R. R. Meier, J. H. Hecht, and A. B. Christensen (1989), Deducing composition and incident electron spectra from ground-based auroral optical measurements: Theory and model results, *J. Geophys. Res.*, *94*, 13,527–13,539.

Strickland, D. J., R. E. Daniell Jr., J. R. Jasperse, and B. Basu (1993), Transport-theoretic model for the electron-proton-hydrogen atom aurora: 2. Model results, *J. Geophys. Res.*, *98*, 21,533–21,548.

Strickland, D. J., J. H. Hecht, A. B. Christensen, and J. Kelly (1994), Relationship between energy flux Q and the mean energy $\langle E \rangle$ of auroral energy spectra based on radar data from the 1987 CEDAR campaign at Sondre Stromfjord, Greenland, disturbance, *J. Geophys. Res.*, *99*, 19,467–19,473.

Strickland, D. J., J. S. Evans, and L. J. Paxton (1995), Satellite remote sensing of thermospheric O/N2 and solar EUV: 1. Theory, *J. Geophys. Res.*, *100*, 12,217–12,226.

Strickland, D. J., R. J. Cox, R. R. Meier, and D. P. Drob (1999), Global O/N2 derived from DE-1 FUV imaging dayglow data: Technique and examples from two storm periods, *J. Geophys. Res.*, *104*, 4251–4266.

Strickland, D. J., J. H. Hecht, A. B. Christensen, and D. J. McEwen (2000), Thermospheric disturbance recorded by photometers onboard the ARIA II rocket, *J. Geophys. Res.*, *105*, 2461–2476.

Strickland, D. J., R. E. Daniell, and J. D. Craven (2001), Negative ionospheric storm coincident with DE 1-observed thermospheric disturbance on October 14, 1981, *J. Geophys. Res.*, *106*, 21,049–21,062.

Strickland, D. J., R. R. Meier, R. L. Walterscheid, J. D. Craven, A. B. Christensen, L. J. Paxton, D. Morrison, and G. Crowley (2004), Quiet-time seasonal behavior of the thermosphere seen in the far ultraviolet dayglow, *J. Geophys. Res.*, *109*, A01302, doi:10.1029/2003JA010220.

Thayer, J. P. (1998), Height-resolved Joule heating rates in the high-latitude E region and the influence of neutral winds, *J. Geophys. Res.*, *103*, 471–487.

Thayer, J. P., J. F. Vickrey, R. A. Heelis, and J. B. Gary (1995), Interpretation and modeling of the high-latitude electromagnetic energy flux, *J. Geophys. Res.*, *100*, 19,715–19,728.

Vallance Jones, A. (1974), *Aurora*, D. Reidel, Norwood, Mass.

Vallance Jones, A. (1992), Historical review of great aurora, *Can. J. Phys.*, *70*, 479–487.

Vallance Jones, A., R. L. Gattinger, P. Shih, J. W. Meriwether, V. B. Wickwar, and J. Kelly (1987), Optical and radar characterization of a short-lived auroral event at high latitude, *J. Geophys. Res.*, *92*, 4575–4589.

Webb, D. F., R. P. Lepping, L. F. Burlaga, C. E. DeForest, D. E. Larson, S. F. Martin, S. P. Plunkett, and D. M. Rust (2000), The origin and development of the May 1997 magnetic cloud, *J. Geophys. Res.*, *105*, 27,251–27,259.

Zhao, X. P., and D. F. Webb (2003), Source regions and storm effectiveness of frontside full halo coronal mass ejections, *J. Geophys. Res.*, *108*(A6), 1234, doi:10.1029/2002JA009606.

M. G. Conde, Geophysical Institute, University of Alaska Fairbanks, 903 Koyukuk Drive, P.O. Box 757320, Fairbanks, AK 99775-7320, USA. (mark.conde@gi.alaska.edu)

E. F. Donovan, Physics Department, University of Calgary, 2500 University Drive, Calgary, AB, Canada T2N 1N4. (edonovan@ucalgary.ca)

D. S. Evans, NOAA Space Environment Laboratory, 325 Broadway, Boulder, CO 80309, USA. (david.s.evans@noaa.gov)

J. H. Hecht and T. Mulligan, Space Science Applications Laboratory, The Aerospace Corporation, M2-259, P. O. Box 92957, Los Angeles, CA 90009, USA. (james.hecht@aero.org; tamitha.mulligan@aero.org)

A. J. Kochenash and D. J. Strickland, Computational Physics Inc., 8001 Braddock Road, Suite 210, Springfield, VA 22151, USA. (ajk@cpi.com; dstrick@cpi.com)

D. Morrison, Johns Hopkins University Applied Physics Laboratory, MP3-W171, 11100 Johns Hopkins Road, Laurel, MD 20723-6099, USA. (danny.morrison@jhuapl.edu)

Y. Murayama, Applied Electromagnetic Research Center, National Institute of Information and Communications Technology, 4-2-1 Nukui-kita, Koganei, Tokyo, 184-8795, Japan. (murayama@nict.go.jp)

F. J. Rich, Air Force Research Laboratory (VSBXP), 29 Randolph Road, Hanscom AFB, MA 01731-3010, USA. (frederick.rich@hanscom.af.mil)

Y.-M. Tanaka, National Institute of Polar Research, 1-9-10 Kaga, Itabashi, Tokyo, 173-8515, Japan. (ytanaka@nict.go.jp)